PREPRINT UCRL-83217

Lawrence Livermore Laboratory

Decay of Deformed and Superdeformed Nuclei Formed in Heavy Ion Reactions

Marshall Blann and Ted T. Komoto

August 1979

This paper was prepared for presentation at the
Twelfth Summer School in Nuclear Physics, Mikołajki, Poland
September 2-14, 1979

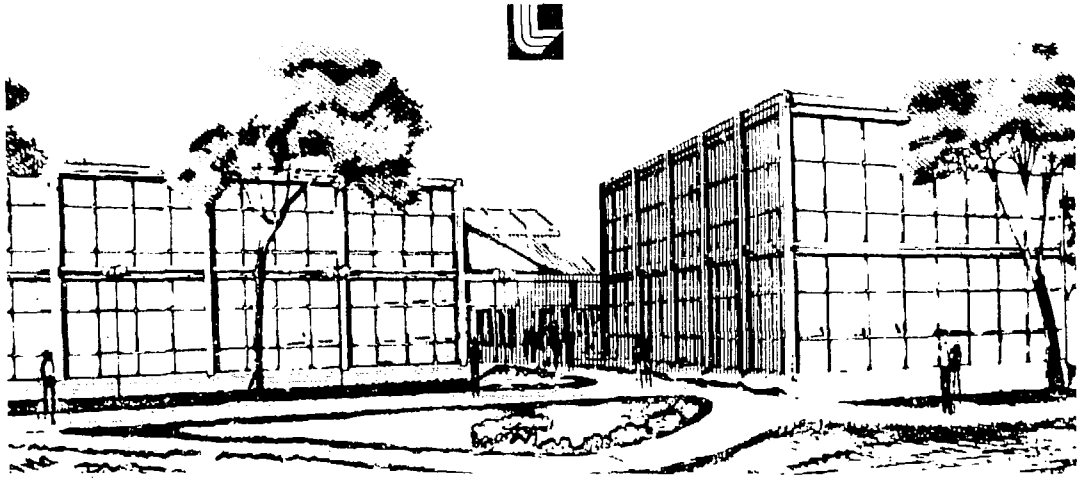

Decay of Deformed and Superdeformed Nuclei Formed in Heavy Ion Reactions*

Marshall Blann
Ted T. Komoto
E-Division, Lawrence Livermore Laboratory
P. O. Box 808, Livermore, California 94550 USA

Lecture notes XII Summer School in Nuclear Physics

*Work performed under the auspices of the U.S. Department of Energy by Lawrence Livermore Laboratory under contract number W-7405-ENG-48.

Abstract

The importance of considering the deformation of nuclei at high angular momenta in computing transmission coefficients for their decay is the major topic of this work. Deformations based on the rotating liquid drop model were used to generate transmission coefficients versus compound nucleus angular momentum. The results were then used in a Hauser-Feshbach code which included fission competition to assess the ultimate importance of deformation modified transmission coefficients. It was found that for a broad range of prolate nuclei (superdeformed) the course of deexcitation predicted changes totally from predominant fission to predominant α decay due to a new mechanism called α decay amplification. The phase space relationships responsible for this new mechanism are presented. It is shown that this predicted new decay mode of superdeformed nuclei is consistent with a large body of existing experimental results, though more explicit experiments must be completed to confirm the new mechanism.

I. Introduction

A large fraction of heavy ion reaction cross sections end up in evaporation residue (ER) and fission-like products. Analyses of these reaction products often involves the statistical model, in various degrees of sophistication (or lack thereof). The degree of agreement between theory and experiment is then interpreted as the reaction being, or not being describable as decay of an equilibrated compound nucleus.

The flaw in this argument of course occurs if the model is used in an invalid form. Indeed the domain of application has been extended, almost without question, from a few tens of MeV of excitation and relatively low angular momenta, to excitations in excess of 100 MeV and angular momenta beyond the predicted limits of stability of the systems in question. Lack of agreement under these circumstances for experimental results versus model calculations may indicate more the inadequacy of the model input than difference in mechanism.

In an earlier work we examined changes in input to the Hauser-Feshbach (HF) statistical approach which might result from relaxation of the Pauli principle due to high excitation energy, and also due to particle emission during the coalescence and equilibration phases of heavy ion reactions.[1,2] In this work we investigate the importance of considering the high deformation of nuclei at high angular momenta in calculating the transmission coefficients (T_ℓ) used as input into statistical codes.[3] The transmission coefficients determine the accessible phase space in the decay process, and can therefore have an exponential influence on final branching ratios.

The nuclear shapes used will be based on the rotating liquid drop model (RLD).[4] They will therefore be of a global nature, and will not reflect

variations due to shell structure; the latter provides a vast area for discussion on its own merit. The very prolate nuclei at high angular momenta will be shown to be dominated by alpha decay, rather than fission, as principle initial deexcitation mode when the ground state deformations are recognized in the T_ℓ input. It will be shown that these results are consistent with many experimental observations, although definitive experiments remain to be done.

A brief review of the RLD will first be presented[4] (Section II), as this model provides the basis for the effort under consideration. Next the statistical calculation itself, and the codes used will be given some discussion (Section III). The calculation of transmission coefficients for spherical and deformed nuclei will be discussed in Section IV. In Section V results of various sets of calculations will be presented, such that the predictions of deexcitation of superdeformed nuclei will be more fully understood, and in particular how these model predictions using T_ℓ for deformed nuclei differ vastly from earlier predictions. Two systems will be calculated for illustrative purposes in order to show the mass dependence of deformation effects. These will be respectively the decay of ^{56}Ni at 172 MeV of excitation as formed by 214 MeV ^{16}O ions on ^{40}Ca, and ^{149}Tb nuclei at 120 MeV of excitation, as formed by 236 MeV ^{40}Ar on ^{109}Ag. Conclusions will be presented in Section VI.

II. Rotating Liquid Drop Model

The rotating liquid drop model of Cohen, Plasil and Swiatecki considers the surface, electrostatic, rotational and total energies for nuclei.[4] These may, following the authors notation, be denoted by E_s, E_c, E_R, and E, with superscript zeros added for the spherical systems.

The energies of the deformed systems are represented with respect to those of the spherical system,

$$B_s(\text{shape}) = E_s/E_s^o$$

$$B_c(\text{shape}) = E_c/E_c^o$$

$$B_R(\text{shape}) = E_R/E_R^o \qquad (1)$$

and the deformation energy is given by

$$\zeta = \frac{E-E^o}{E_s^o} = \frac{E_s-E_s^o+E_c-E_c^o+E_R-E_R^o}{E_s^o}$$

$$= (B_s-1) + 2 \times (B_c-1) + y(B_R-1) \qquad (2)$$

In Eqs. (1),

$$E_s^o = 4\pi R^2\gamma$$

$$E_c^o = \frac{3}{5}\frac{Q^2}{R}$$

and

$$E_R^o = \frac{1}{2}\frac{L^2}{\frac{2}{5}MR^2} \qquad (3)$$

where R is the spherical radius, M the total mass, L the angular momentum, Q the charge and, γ is the surface tension coefficient.

The x and y parameters of Eq. (2) specify respectively the ratios of electrostatic and rotational energies of the sphere to the surface energy E_s^o,

$$x = \frac{E_c^o}{2E_s^o}$$

$$y = \frac{E_R^o}{E_s^o} \qquad (4)$$

It can be seen that y is a function of the square of the angular momentum, and therefore a measure of the tendency toward deforming the rotating nucleus with respect to the restoring surface energy. The parameter x is the well known "fissility" parameter. The RLD presentation of equilibrium configurations is in terms of the parameters x and y.

Figure 1 shows the x-y plane divided into three regions, y_I, y_{II}, y_{III}.[4] The y_{III} curve represents the region below which the fissioning system ceases to be stable against asymmetry. Below y_I equilibrium shapes are oblate; between y_I and y_{II} they are prolate or triaxial, and beyond y_{II} the nuclei are unstable against fission.

Figures 2 and 3 show some shape projections for nuclei near those to be used as sample systems in this work, ^{56}Ni and ^{149}Tb. Note the very large radii for the prolate nuclei at larger y values.

Quantitative relationshps of principal axes versus x and y, the results which were used in this work,[4] are shown in Fig. 4. The ordinate is relative to the radius of the spherical nucleus; the fissility parameter is the abscissa, and y values are shown for a series of numbers between zero and 0.72. The nearly horizontal lines above 1.0 on the ordinate are for the major axis of the oblate shapes. The more vertical intersecting curves (above 1 on the ordinate) represent the principal axes of the prolate shapes. The

lower near vertical curves extending from the R > 1 intersections give the median axes of the triaxial shapes, and the R < 1 intersecting curves the minor axes. When the near vertical curves bend back into the horizontal position, they represent the major, median, and minor saddle point axes.

Figure 4 was used with interpolation in determining the ground state equilibrium shapes on which this work is based. The major axes were used from Fig. 4; it was assumed that minor and median axes were equal.

We should close this section with a direct quote from the original reference: "One comment should be made about the expected accuracy of the graphs in Figs. 10 to 13. For the axially symmetric Hiskes shapes all results are essentially exact; on the other hand for the triaxial shapes there are substantial inaccuracies, especially in the plots of the axes and moments of inertia. Without going into the details of the approximations underlying the calculations of the triaxial figures we may say that we consider the graphs as adequate semi-quantitative guides for the discussion of those shapes, but that calculations of their properties with controlled and high accuracy is still a project for the future on which we hope to report at a later date."[4] (p. 30, LBL 1502).

The latter quotation should serve both to put this work into perspective, and as food for thought for those who interpret RLD fission barriers as being a priori of extremely high accuracy.

III. Comparison of Statistical Decay Models and Codes Used.

A. General comparisons of model formulations

Several statistical model codes are in use for treating the deexcitation of highly excited nuclei. A tradeoff is generally to be found in speed versus sophistication in going from codes such as ALICE,[5] to codes such as MBII.[6] At this point a few words may be in order to outline what the tradeoffs are between several of these codes. The idea is to choose the quickest code and options which will provide an answer as accurate as needed. The codes to be described were written to be quite versatile and flexible, and there is no universal answer to the question as to which code to use.

First let us summarize the basic equations which one uses in these and similar codes, in greater or lesser degrees of sophistication. The symbols are summarized in Table 1. First consider the angular momentum dependent Hauser-Feshbach (HF) version

$$P_\nu(\varepsilon,I)d\varepsilon = \frac{(2s_\nu+1)\sum_{\ell=0}^{\infty} T_\ell^\nu(\varepsilon) \sum_{J=|I-\ell|}^{I+\ell} \rho(U,J)d\varepsilon}{\int_{\varepsilon=0}^{\infty} \sum_{\nu=1}^{n}(2s_\nu+1)\sum_{\ell=0}^{\infty} T_\ell^\nu(\varepsilon) \sum_{J=|I-\ell|}^{I+\ell} \rho(U,J)d\varepsilon} \qquad (5)$$

where symbols are defined in Table 1.

The meaning of this equation may be illustrated by reference to Figure 5. Here we show an E versus J plane of a residual nucleus. The region is shown below the yrast line into which no particle emission is possible.

It is instructive to appreciate the dependence of the nuclear level density in the space of excitation energy and angular momentum. This is shown qualitatively in Fig. 5. The yrast and saddle point lines are indicated (for ^{56}Ni) and two "cuts" through the space are shown. One of these -A- is at constant excitation. For this case the level density increases as 2J+1 with increasing J until the rotational energy becomes significant, at which point there is an exponential decrease as one approaches the yrast angular momentum at fixed excitation.

In the second cut -B- the exponential dependence of the level density on the square root of excitation energy above the yrast energy is shown. The branching in deexcitation is pretty much determined by the level densities. It may be seen that emission is greatly decreased if it is forced to be near the yrast limits, and greatly enhanced if populations far from yrast limits can be populated.

In the results to be presented we have used a spin dependent level density as proposed by Lang,[7]

$$\rho(E,J) \propto (2J+1)E^{-2} \exp 2\sqrt{a(E-E_{ROT}(J))} \qquad (6)$$

Lang showed that this expression, which naturally has no level density below the yrast line, is vastly superior to the more common exponential cutoff factor formulation.

The steepness of the yrast line, and therefore of the spin cutoff region, is an important consideration in deciding which of several formulations to use. In Figures 6 and 7 we have drawn the yrast line on an E versus J plot to show the mass dependence, using as examples mass numbers 56 and 149. The yrast lines were taken from the rotating liquid drop model.

In Figures 5 and 7 a region of possible particle emission may be found for which decrementing the excitation energy by the particle binding energy leaves the nuclei in an excitation region below the yrast line (if $\Delta J=0$). It may be seen that each mass system requires a different number of partial waves to reach the region for which levels exist. The number of l waves available to n,p and α particles for each mass and angular momentum region will in general determine the sophistication of formulation required.

Consider the case often encountered in higher mass nuclides, where only neutron emission is important. Assume that since very few partial waves can be carried by the neutrons, that the initial and final spin distributions are unchanged. This has been called the s-wave approximation.

With this assumption, eq. (1) may be rewritten

$$P_\nu(E,I)d\varepsilon = \frac{(2s_\nu+1)\sum_{\ell=0}^{\infty}(2\ell+1)T_\ell^\nu(\varepsilon)\ \rho(U,I)d\varepsilon}{D} \tag{7}$$

where D is the normalization denominator similar to that in eq. (5). This in turn may be seen to be equivalent to

$$P_\nu(E,I) = \frac{(2s_\nu+1)\ \rho(U,I)\ \cdot\ \mu\varepsilon\sigma_\nu(\varepsilon)}{D} \tag{8}$$

when the substitution is made

$$\sigma_\nu(\varepsilon) = \pi\lambda^2\sum_{\ell=0}^{\infty}(2\ell+1)T_\ell \tag{9}$$

Equation (8) is the s-wave approximation used in the code ALICE;[5] it may be seen that the factorization made possible by assuming no change in the I distribution changes the HF form into the Weisskopf s-wave form (eq. 8), which for an infinite moment of inertia reduces to

$$P(\epsilon) \propto (2s_\nu + 1)\, \epsilon\, \rho(U)\, \mu\epsilon\sigma_\nu(\epsilon)d\epsilon \qquad (10)$$

ALICE allows calculation with either (8) or (10). The difference may be seen on the E-J diagram of Figures 6 and 7; the s-wave approximation implies that all rotational energy will eventually be dissipated by γ-ray cascade, since outgoing particle l waves cannot couple to lower J (vertical lines for each J would indicate final J loci). The Weisskopf[8] formula (10) results from (8) when an infinite moment of inertia is assumed, which implies zero rotational energy and zero yrast energy.

The s-wave approximation may be seen to be good when the outgoing particles cannot carry off many partial waves, and when the yrast line is not terribly steep. It is useful in giving the broadening of excitation functions due to angular momentum and the increased γ-ray deexcitation due to this cause. It cannot give the emission enhancement effects expected for α particles due to higher partial waves accessible in the exit channel. It overestimates the energy in the γ-ray cascade, and therefore also the broadening of excitation functions. Its running time is likely to be of the order of 1% or less that of MBII e.g., the HF code, for the comparable calculation. Comparisons illustrating these points and comparing the several statistical formulations may be found in Ref. 9.

If one is interested in excitation function analysis for isotope production at $A > 100$, the s-wave approximation would likely be the choice (e.g. as in ALICE). For reactions in $A = 200$ nuclei with $I \leq 60$, the Weisskopf calculation would be adequate for product cross sections. If, however, one works in light mass systems, or is interested in details of angular momentum distributions, then a HF type calculation is recommended.

In the remainder of these notes, we will indicate a probable additional inadequacy of all previous HF calculations when applied to nuclei at very high I, such as those which are commonly produced in heavy ion reactions. No discussion is given herein as to the inclusion of the fission channel in the statistical decay models, as this point has been covered in detail in ref. 2.

B. Code Properties - ALERT

The code used for the calculations to be presented represents a minor modification of the MBII code;[6] the new code has been named ALERT. The logic of the code is represented pictorially in Fig. 8. The computer core recognizes files corresponding to a chart of nuclides like region beginning with the compound nucleus at some excitation energy E, and with a partial reaction cross section distribution σ_I. The subroutines used to provide input to the HF calculation will be described shortly.

The ALERT code nuclides are each dimensioned 100 $\hbar$ x 200 MeV with a mesh size 1 MeV by 1 $\hbar$. Outgoing particles (n,p,α) may have energies to 60 MeV and angular momenta to 60 $\hbar$, also with 1 MeV and 1 $\hbar$ mesh size. The gamma-ray competition with particle emission has been limited arbitrarily to 15 MeV above the yrast energy at each value of the angular momentum. At present an array 9 mass units wide by 7 Z units deep may be calculated (63 nuclides), although these dimensions could easily be extended.

As is illustrated in Fig. 8, n,p,α, fission, and sometimes γ emission spectra are calculated, and the residual nuclide differential cross section elements are stored in the appropriate residual nuclide array. The particle emission spectra are also stored according to kinetic energy and angular momentum of the outgoing particles.

When no further particle emission or fission is possible from the compound nucleus, control transfers to the nucleus A-1,Z; this becomes the new compound nucleus, and the deexcitation calculation is continued for as many of the 20,000 E-J points as may be populated and capable of further deexcitation. The calculation continuous to A-2, etc., then to A-1, Z-1, A-2, Z-1, etc. until all nuclides in the array specified by data input have had their population and deexcitation calculated.

The code has been written to read transmission coefficients from either an internally generated or separately generated files. Binding energies and Q values may be user supplied or internally generated using the Myers-Swiatecki Lysekil mass formula.[5,10] Fission barriers and ground state rotational energies are generated using the RLD,[4] with subroutines from the code ALICE;[5] entrance channel T_ℓ are calculated from the parabolic model routine from code ALICE.[5,11]

IV. Calculation of Transmission Coefficients for Spherical and Deformed Nuclei

A. Spherical nuclei

Standard global optical model parameter sets from the MOII code subroutines were used to generate T_ℓ sets for nuclei beginning with the compound nucleus (A,Z) and for nuclides (A-2, Z-1)----(A-10, Z-5).[6,12] This was done for n,p, and α particles at channel energies between 0.1 MeV and 59.1 MeV in 1-MeV increments. Partial waves up to 60 $\hbar$ were permitted in the buffers chosen.

Classical sharp cutoff parameters (SCO) were also selected to reproduce, as nearly as possible, the optical model results. The sharp cutoff model T_ℓ values were defined by

$$\ell_{max} = 0.187\sqrt{2\mu\varepsilon}\,(R_\nu + 3.4/\varepsilon^{1/2}) \qquad (11)$$

For neutrons and

$$\ell_{max} = 0.187\ \sqrt{2\mu\varepsilon}\ \sqrt{1-V_{\nu,i}/\varepsilon} \tag{12}$$

for protons and α particles, where

$$T_\ell\ (\varepsilon) = 1 \text{ if } \ell \leq \ell_{max}$$

$$T_\ell\ (\varepsilon) = 0 \text{ if } \ell \geq \ell_{max} \tag{13}$$

The radius R_ν is defined by

$$R_\nu = 1.21\ ((A-A_\nu)^{1/3} + A_\nu^{1/3}) \tag{14}$$

and the potential by

$$V_\nu = \frac{(Z-Z_\nu)Z_\nu K_\nu}{(R_\nu + 1.6)} \quad \text{MeV}, \tag{15}$$

where $K_\nu = 1.32$ for α particles and 1.15 for protons. A comparison between the SCO result and the optical model result is shown in Fig. 9 for 30 MeV α particles incident on $^{52}_{26}$Fe. Results for neutrons and protons as calculated on the SCO are shown in Fig. 10.

B. Deformed nuclei

The rotating liquid drop model (Fig. 4) was used to estimate the maximum radius of the equilibrium deformed nucleus at various values of the angular momentum. Calculations were performed for each nucleus for I = 5 h to I = 95 h in 10 $\hbar$ increments. If the deformation exceeded the saddle point value, the saddle point result was taken. The latter procedure requires some discussion. First, calculation of input T_ℓ for nuclei with angular momenta beyond the RLD stability limit does not require that this regime be considered in any particular de-excitation calculation. However, if the intrinsic excitation equilibration

and particle emission decay rates are much greater than the rate of fission, such a calculation may give valuable insights into the possible non-equilibrium decay modes.

Two procedures were followed for generating sets of transmission coefficients for deformed nuclei. One of these involved an averaging over the surface of the spheroid indicated by the RLD using the classical SCO approximation; the other was an extreme model in which the optical model radius was modified to generate T_ℓ results appropriate for emission from the tips of the nuclei.[3]

In the classical SCO approximation the triaxial shapes were replaced by ellipsoids of revolution having a major axis to spherical axis ratio as given by RLD, and a minor axis defined to be volume conserving. The spheroids of revolution were defined by

$$\frac{x^2}{c^2} + \frac{y^2}{a^2} = 1 \tag{16}$$

where x is the symmetry axis and y is 90° to x.

The potential of such a spheroid at any point on the surface is given by[13]

$$V(x,y) = D - 1/2\ Ax^2 - 1/2\ By^2 \tag{17}$$

where

$$D = \frac{3Z}{2c} K \tag{18}$$

$$A = \frac{3Z}{\varepsilon^2 c^3} [K-1] \tag{19}$$

$$B = \frac{3Z}{2\varepsilon^2 c^3} [\frac{1}{(1-\varepsilon^2)} - K] \tag{20}$$

$$K = \frac{\ell n[(1+\varepsilon)/(1-\varepsilon)]}{2\varepsilon} \tag{21}$$

and

$$\varepsilon = \sqrt{1-a^2/c^2} \tag{22}$$

The eccentricity ε is real if a prolate spheroid and imaginary if an oblate spheroid.

The transmission coefficients were then defined as to the ℓ_{max} at the surface of the spheroids at increments in radius where the maximum radii R_ν of Eq. (14) were replaced by

$$R' = \frac{R_{max}}{R_0} R_\nu \tag{23}$$

The symmetry axis was divided between zero and R' into 50 increments. For each increment the surface area was approximated by

$$\Delta A_i \cong 2\pi y_i S_i \tag{24}$$

where

$$S_i = \sqrt{(y_i - y_{i-1})^2 + (\Delta x)^2} \tag{25}$$

(and $\Delta x = 0.02$ c). The potential V_ν of Eq.(15) was replaced by $V_{\nu,i}$ calculated for $(x_i;y_i)$ of each segment according to Eq. (17). The variation of V(x,y) and R with x increment is shown in Fig. 11. The T_ℓ values were then averaged over the surface area by

$$T_\ell(\varepsilon) = \sum_{A_i} \frac{\Delta A_i}{A_i} \delta_\ell \tag{26}$$

where $\delta_\ell = 1$ if $\ell \leq \ell_{max}$ and $\delta_\ell = 0$ if $\ell > \ell_{max}$.

A comparison between the T_ℓ values calculated for α particles for a spherical and deformed nucleus via the SCO and optical models is shown in Fig. 9. A comparison of SCO model results for neutrons and protons for spherical and deformed nuclei is shown in Fig. 10.

In Fig. 9, the deformed optical potential result is shown for α particles. The optical model radii were modified by multiplying the radius parameter r_o by R_{max}/R_o. The diffuseness parameter was left unchanged. The ratio of coulomb barriers at the tip of the deformed nucleus to that at a point on the ground state spherical nucleus was computed, and the charge of the optical model was altered to reproduce the calculated barrier height at the enlarged radius. This represents an extreme estimate of the effect to be expected from deformation. Comparisons between results using the SCO and optical model results might therefore give some indication as to whether results are very sensitive to the exact manner in which the T_ℓ are calculated, or only to the fact that the deformation is included in some fashion in determining the T_ℓ cutoff point.

The averaged SCO results may be seen to give T_ℓ values which begin to cut off at lower ℓ than the non-deformed SCO. This reflects the lower radii at the 'waist' of the highly deformed nuclei. The averaged SCO results are generally lower than the extreme deformed optical results, as expected. Yet it will be shown that results are not terribly sensitive as to which T_ℓ set is used. The relative shapes, and coulomb barriers as a function of angular momenta are summarized in Figs. 12 and 13 for the two sample systems (^{56}Ni and ^{149}Tb) considered in the work. It may be seen in these figures that the superdeformed region is entered quite rapidly once the transition to prolate shapes is made, and that a considerable reaction cross section exists for superdeformed nuclei with nonzero fission barriers.

IV. Results of Statistical Decay Calculations for Deformed versus Spherical Nuclei

A. E-J plane phase space comparisons

In order to appreciate results to be presented, it is worthwhile to examine the E-J space of the residual nuclei. This is shown in Figs. 6 and 7.

The point of compound nucleus excitation is shown for each test system ($^{149}_{65}$Tb and $^{56}_{28}$Ni) for a single value of the entrance channel angular momentum, in each case for a superdeformed nucleus. Residual U and J are considered for α particle emission. There is an energy required for α binding energy and for the coulomb barrier. For each value of the kinetic energy, there is a maximum ℓ value which the outgoing particle can use to couple to lower (or higher) angular momenta. The loci of ℓ_{max}, coupled antiparallel with I, are shown in Figs. 6 and 7, for the α kinetic energy range from the coulomb barrier to 39 MeV. The loci are shown for the SCO model for both spherical and for deformed nuclei. The results of this figure using optical model T_ℓ values are essentially identical.

The consequences of using deformed versus spherical transmission coefficients may be understood qualitatively by comparing the loci of minimum residual angular momenta for the two cases. The n and p channels (cf Fig. 10) do not show such a large change in T_ℓ between spherical and deformed nuclei as do α particles, and deformation effects on fission rates are already explicitely considered via the RLD saddle point energy. The main change in deexcitation properties results from the enhanced α emission due to the much higher effective residual excitation accessible when deformation effects persist.

For the ^{149}Tb case, the residual nucleus excitation range for emission of 9 to 39 MeV α particles is 60 to 41 MeV for spherical T_ℓ, and 74 to 59 MeV when deformed T_ℓ are considered. Since these energies enter the level densities in an exponential way, a huge effect is to be expected. As a many fold enhancement of α decay results, we refer to this as an α decay amplification.

An even more dramatic, qualitatively different result obtains for the ^{56}Ni compound nucleus. Here the steepness of the yrast line permits the result that as the α emission energy from the deformed nucleus goes from 8 to 39 MeV, the accessible residual excitation actually increases from 89 to 107 MeV! In contrast the excitation range decreases for the spherical case from 79 to 75 MeV over the same range. From these numbers one can see that α decay is enhanced over results at lower angular momenta using spherical T_ℓ, but should be very strongly enhanced for deformed versus spherical T_ℓ at high angular momenta. In this example an additional 30 MeV of residual excitation is available to the deformed system. The very large effect here might be called a superamplification from superdeformed nuclei. We turn next to quantitative results of these qualitative considerations.

B. Decay Branching Ratios and Amplification Factors

Branching ratios for first chance particle emission and for total fission deexcitation are summarized in Fig. 14 for ^{149}Tb and in Fig. 15 for ^{56}Ni. Results are compared for both spherical and deformed T_ℓ.

In each case nucleon emission exceeds other decay modes at low angular momenta. Consider the 'spherical' T_ℓ emission as angular momentum increases. The α emission probability initially increases with increasing I, as expected. Perhaps less anticipated is the subsequent decrease as angular momentum increases further. It may be seen that this is a consequence of the rapid increase in the fission width with increasing I. It illustrates as a side point the importance of including the fission channel in HI deexcitation calculations, e.g., to compute residual angular momentum distributions. At higher excitations fission completely dominates the deexcitation. There should be no evaporation residues according to the spherical T_ℓ calculation.

Next compare the branching ratios when T_ℓ of deformed nuclei are used (the SCO model results were used in preparing Figs. 14 and 15). In both these cases the additional phase space available for α decay causes a huge increase in its emission rate such that this mode totally dominates the decay process: total fission drops to around 1% for ^{56}Ni at 55 ħ, down from 74%, and to 10% for ^{149}Tb, down from 97%. The full liquid drop fission barriers were used in all the calculations, and $a_f/a_\nu = 1.0$ was assumed.

Numerical results of Figs. 14 and 15, with additional information are summarized in Tables 2 and 3. Results for ^{149}Tb deexcitation are summarized in Table 4 for T_ℓ computed with the optical model as described in Section IV. In particular it is of interest to compute the α decay amplification factor due to deformation. This amplification effect may be expressed in a quantitative fashion if it is assumed that the change in n and p decay rates due to using T_ℓ characteristic of deformed rather than spherical nuclei is negligible. One can then represent the fractional α decay from spherical or deformed nuclei as f_α^s and f_α^d, respectively; the rates of α-decay as R_α^s and R_α^d, and the rate of n,p, and fission decay by R. The fraction of α-decay from spherical and deformed nuclei can then be represented as

$$f_\alpha^i = \frac{R_\alpha^i}{R_\alpha^i + R}\ , \quad i = s \text{ or } d \quad . \tag{27}$$

Then the amplification factor A, defined as the ratio of α-decay rates for the deformed versus spherical system is given by

$$A = \frac{R_\alpha^d}{R_\alpha^s} \quad \frac{f_\alpha^d(1-f_\alpha^s)}{f_\alpha^s(1-f_\alpha^d)} \tag{28}$$

It may be seen in Table 2 (and 3) that the α amplification for ^{56}Ni (^{149}Tb) starts to become significant above 35 ħ (65 ħ), exceeding a factor of

65 (40) by 55 ħ (35 ħ).

The phase space increase may be seen to cause such an increase in α emission rate that the predicted fission fate of the high I compound nuclei is highly suppressed. Furthermore, following the dominant α decay mode in the first step of deexcitation, the residual nuclei are at very much lower J than would have been expected. This means that nuclei formed near (and perhaps beyond) the barrier disappearance point could α decay to a nuclide having a significant fission barrier. This nuclide might in turn undergo fission, or deexcite to an ER by further particle emission.

Some comparisons might be made at this point to some relevant, but probably inconclusive experimental results. Vigdor et al. have measured the ER excitation function for $^{16}O + ^{40}Ca$ at energies up to and including 214 MeV.[14] They report that there is no evidence of fission for the system, with ER yields implying ℓ_{fus} of $\gtrsim 54$ ħ. This is consistent with the calculation using T_ℓ for deformed nuclei, inconsistent with the result using spherical T_ℓ values.

Additional comparisons are to be found in experimental results published by Britt et al.[15,16] One set involves the system $^{40}Ar + ^{109}Ag$ at incident ^{40}Ar energies of 169 to 337 MeV (lab).[15] Evaporation residue and fission-like excitation functions were measured. The sum of fission-like and ER cross sections imply fusion angular momenta beyond the liquid drop limit. This could have several interpretations. One of these is that the fission-like yields measured (and reported to have some ambiguity of interpretation) are from a non-compound mechanism. Another is that the predicted initial α decay takes place, leaving a residual nucleus with finite fission barrier which then undergoes fission. This is very speculative on such weak evidence of course; more direct experiments are suggested.

Additional evidence--still not conclusive--is to be found in yet another result of Britt et al.[16] reproduced as Fig. 16 herein with the kind permission of at least one of the co-authors. In Fig. 16 the ℓ_{max} determined from γ-ray multiplicity measurements is shown as a function of excitation energy. The systems included are $^{40}Ar + ^{122}Sn$, $^{86}Kr + ^{76}Ge$. This curve seems to flatten at around 65 h. This could result from the fission limit, except that the σ_{ER} results imply yet higher ℓ limits. (The latter also include points from ^{86}Kr and Cu and $^{40}Ar + ^{121}Sb$.) This may also be seen in the ℓ_{max} from ER measurements in Fig. 16. They clearly extend beyond the survival range expected for I, when deexcitation fission competition is included in the decay calculation. Both sets of results are consistent with deexcitation by α amplification at high angular momenta. The residual angular momenta are seen to limit around 65 $\hbar$ following emission of the first α particle (Tables 3,4) from the superdeformed region consistent with the γ-ray multiplicity results. This would also stabilize the residues against subsequent fission, consistent with the higher ℓ_{max} deduced from the σ_{ER} results (since the latter are inferred from the cross sections surviving fission deexcitation, whereas the γ-ray multiplicity is a measure of the actual angular momentum of the evaporation residues following particle emission.)

Another result consistent with the change in deexcitation to be expected by consideration of deformation is found in product yield measurements. Plasil et al.[17] (and others as well) have found in measuring the nuclidic yields of evaporation residues, that more charged particles are apparently emitted than are predicted by ordinary evaporation theory. As Figures 14 and 15 indicate, the superdeformation should enhance the charged particle emission substantially. This represents yet another observation consistent with the proposed new mechanism, yet still is inconclusive.

C. Kinetic Energy Spectra

The influence of superdeformation on the α kinetic energy spectra is shown in Tables 2-4 and in Figs. 17 and 18. The most probable energies are summarized in the tables. For ^{149}Tb, spherical T_ℓ calculations predict a reasonably invariant most probable kinetic energy with I, whereas deformed T_ℓ values predict some increase at the higher I values. For the case of ^{56}Ni, the spherical T_ℓ results predict most probable kinetic energies of 13-20 MeV for I = 0 to 45 ħ, then decreasing to 13 MeV. For the deformed case, the most probable energy continued to increase monotonically to 36 MeV at 55 ħ! This represents nearly a factor of two increase in peak kinetic energy over the spherical result. It may be seen in Fig. 18 that the superamplified α particles from ^{56}Ni are expected to extend with reasonable cross sections to energies up to 60 MeV, from a purely evaporation, non-precompound mechanism! This represents a rather surprising change from results of all earlier calculations for which spherical T_ℓ values were used.

The high energy α particles are predicted to set in rather sharply in ^{56}Ni beyond 35 ħ as the superdeformed region is populated (see also Figs. 12 and 13). Vigdor et al.[14] measured ER angular distributions at a series of bombarding energies. They observe a bulge and extension to relatively high recoil angles at bombarding energies where the predicted superdeformed region is populated. Kinematic calculations show that the emission of one or two energetic α particles or a Be^8 emission could well explain this bulge. The deformed nucleus calculation would predict large ^{8}Be emission cross sections, whereas the spherical case would not. A coincidence experiment is presently being pursued by the Livermore heavy ion group to measure the spectrum of the light particles emitted in coincidence with the heavy fragment.

D. Multiple Particle Emission Patterns

It is of some interest to see how the total deexcitation pattern varies for the various T_ℓ inputs under discussion. Figures 19-22 indicate the particle emission cross sections for deexcitation by the n,p,α and fission channels for a ^{56}Ni compound nucleus initially populated at 55 $\hbar$. The results are shown using SCO T_ℓ values for both spherical and deformed nuclei. Results are also shown using optical model T_ℓ for spherical nuclei, and the optical model tip emission assumption for deformed nuclei. In Fig. 24 a result is shown at 45 $\hbar$ using the SCO for deformed nuclei.

For both sets of spherical T_ℓ (SCO Fig. 19 and optical model Fig. 20) very similar deexcitation patterns are predicted. In each case first chance fission is comparable to all other decay channels, as is α decay. In both cases fission accounts for 75% of the deexcitation when multiple particle emission is considered. Nucleon emission is in both cases the dominant overall non-fission mode of deexcitation.

Next consider the two sets of results (Figs. 21 and 22) using deformed T_ℓ values. In each case total fission falls to below 0.5% for first chance fission, and below 1% over all channels, independent of the T_ℓ set used. In each case first chance α decay accounts for at least 95% of the decay. And in each case second and third alpha particles are of the same order of magnitude as nucleon emission. The similarities of results from the two sets of calculations with deformed nuclei again emphasizes that the α decay amplification is not strongly dependent on how the T_ℓ are calculated, but rather result from recognizing that the deformation and large radii do exist, and that this allows some high partial waves for the emitted α particles. Figure 23 shows that the α amplification and fission suppression persist strongly at 45 $\hbar$, as is shown by reference to Table 2.

IV. Conclusions

We have stressed that the RLD which seems to properly and semi-quantitatively predict the disappearance of the fission barrier with high angular momenta, also predicts very high equilibrium deformations for rotating nuclei in their ground states. We further show that consideration of this deformation makes substantial changes in transmission coefficients for particle emission, particularly for α particles.

Since residual excitation has an exponential influence on level densities, the predicted change in T_ℓ values for deformed nuclei leads to a strong amplification of α decay. This in turn can totally alter the predicted course of deexcitation at high angular momenta from almost pure fission to almost pure α decay, and can quantitatively alter the cross section and J distribution of ER products surviving fission.

Many of the predicted changes expected in statistical deexcitation due to including deformation effects, are consistent with a broad body of experimental evidence. Many experiments which might more directly verify the model predictions are implicitely suggested, and some of these are underway. Since the deformation of nuclei at high angular momenta has been verified by a huge body of evidence, it is not so reasonable to ask for a justification of the model presented herein, as for all the previous calculations using T_ℓ computed for spherical nuclei!

As there is evidence for a rapid energy equilibration in the entrance channel of heavy ion reactions,[18] the phase space considerations stressed herein may also prove valuable in addressing deexcitation of interacting heavy ion/target systems prior to the attainment of equilibrium, i.e., for various possible precompound modes of deexcitation. We feel that this model, and the

predicted new mechanism of α decay amplification from superdeformed nuclei merits further testing and exploration, as it is potentially important in understanding HI reaction mechanisms.

The author has appreciated valuable discussions with Dr. W. J. Swiatecki and Dr. M. Beckerman during the course of this work.

Table 1. Definition of symbols used.

T_ℓ, $T_\ell(\varepsilon)$, $T_\ell^\nu(\varepsilon)$	Transmission coefficient; for channel energy ε; for particle type ν and orbital angular momentum ℓ $\hbar$.
$P_\nu(\varepsilon,I)d\varepsilon$	Probability of emitting particle type ν with channel energy ε to $\varepsilon + d\varepsilon$ from compound nucleus of angular momentum I.
s_ν	Intrinsic spin of particle ν.
E	Compound nucleus excitation.
U	Residual nucleus excitation.
J	Residual nucleus angular momentum.
ℓ	Orbital angular momentum of captured or emitted particle.
$\rho(U,J)$	Level density of nucleus at excitation energy U and angular momentum J.
α	Level density parameter; value used in this work is A/10 MeV^{-1}.
$E_{ROT}(J)$	Rotational energy of a nucleus with angular momentum J ($\hbar$).
μ	Reduced mass.
$\sigma_\nu(\varepsilon)$	Inverse reaction cross section for particle ν with channel energy ε.
σ_{ER}	Evaporation residue cross section.
ER	Evaporation residue.

Table 2. Summary of $^{56}_{28}Ni$ decay at 160-MeV excitation using sharp cutoff transmission coefficients for spherical and deformed nuclei.

	Spherical				Deformed			
$I(\hbar)$	5	35	45	55	5	35	45	55
$\sigma(I)$	4.1	26.7	34.2	41.7	4.1	26.7	34.2	41.7
f_n [a]	.30	.21	.20	.22		.21	.056	.018
f_p	.50	.36	.37	.44		.33	.11	.042
f_α	.21	.43	.40	.17		.46	.82	.93
f_f [b]	0	.0036	.035	.17		.003	.007	.009
f_f [c] total		.006	.094	.74		.005	.008	.010
Amplification for α decay						1.13	6.8	65.
ε_α [d] (mp)(MeV)	13	18	20	13	13	19	28	36
$\langle J_\alpha \rangle$ [e] $\hbar$		28.5	36.4	49.7	--	26.2	25.4	24.5
$\langle J_n \rangle$ [f] $\hbar$	5.6	32.7	43.1	53.7	5.6	32.5	41.5	51.9

a) fraction decay by neutron channel

b) first chance fission fraction

c) total fission fraction with multiple emission

d) most probable kinetic energy

e) average final angular momentum following emission of one α particle

f) average final angular momentum following emission of one neutron

Table 3. Summary of $^{149}_{65}Tb$ decay at 120 MeV excitation using transmission coefficients for spherical and deformed nuclei calculated in the sharp cutoff approximation. Liquid drop barriers were used.

	Spherical					Deformed			
I(h)	5	65	75	85	95	65	75	85	95
$\sigma(I)$	1.43	17.0	19.6	22.2	24.8	17.0	19.6	22.2	24.8
f_n	.70	.65	.59	.50	.44	.62	.43	.090	.11
f_p	.12	.079	.064	.05	.040	.075	.051	.0135	.017
f_α	.18	.26	.25	.13	.077	.29	.45	.86	.80
f_f	0	.009	.097	.320	.44	.009	.064	.040	.074
f_f^{total}	0	.058	.52	.93	.97	.049	.52	.090	.165
Amplification for α decay						1.16	2.4	41	48
ε_α(mp)	18	18	18	18	18	21	21	23	24
$\langle J_\alpha \rangle$	7.0	58.8	68.0	79.7	97.4	58.4	64.2	56.9	65.6
$\langle J_n \rangle$	5.7	63.4	73.4	84.3	93.8	63.2	73.0	83.1	92.8

Table 4. Summary of $^{149}_{65}Tb$ decay at 120-MeV excitation using transmission coefficients for spherical and deformed nuclei calculated using the nuclear optical model.

$I(\hbar)$	5 [a]	65	75	85	95	55	65	75	85	95
	Spherical Nuclei					Deformed Nuclei				
$\sigma(I)$ mb	1.43	17.0	19.6	22.2	24.8	14.4	17.0	19.6	22.2	24.8
f_n	.63	.49	.33	.23	.19	.53	.45	.21	.037	.052
f_p	.11	.065	.040	.025	.020	.084	.065	.033	.009	.015
f_α	.25	.31	.23	.10	.058	.35	.37	.62	.92	.88
f_f [b]	.0014	.139	.40	.64	.73	.038	.12	.14	.032	.056
f_f total	.0014	.56	.87	.97	.99	.17	.46	.49	.38	.47
Amplification for α decay							1.3	7.4	104	120
ϵ_α(mp) (MeV)	21	21	21	20	19	21	21	21	23	24
J_α [c](mp) $\hbar$	-	59	68	80	92	49	58	63	63	67

a) This column is characteristic of spherical nuclei at zero angular momentum; column 6 for 55 $\hbar$ should be approximately characteristic of spherical systems as well, since deformations are not large at 55 $\hbar$.

b) Liquid drop fission barriers reduced by 40% were used with $a_f/a_\gamma = 1.03$.

c) Most probable residual angular momentum following the emission of one α particle.

References

1. M. Blann, A. Mignerey and W. Scobel, Nukleonika 21 (1976) 335.
2. M. Blann and M. Beckerman, Nukleonika 23 (1978) 1.
3. M. Beckerman and M. Blann, Phys. Rev. Lett. 42 (1979) 156.
4. S. Cohen, F. Plasil and W. J. Swiatecki, Ann. Phys. (N.Y.) 82 (1974) 557; Report LBL 1502 (1972).
5. M. Blann and F.Plasil, Report COO-3494-10 (1973) (unpublished); M. Blann, Report COO-3494-29 (1977) (unpublished); F. Plasil, Report ORNL/TM-6054 (1977)(unpublished).
6. M. Beckerman and M. Blann, Report UR-NSRL-135A (1977) unpublished.
7. D. W. Lang, Nucl. Phys. 77 (1966) 545.
8. V. F. Weisskopf, Phys. Rev. 53 (1937) 295.
9. M. Blann, Phys. Rev. 157 (1967) 860.
10. W. D. Myers and W. J. Swiatecki, Ark. Fys. 36 (1967) 343.
11. T. D. Thomas, Phys. Rev. 116 (1959) 703.
12. D. Wilmore and P. E. Hodgson, Nucl. Phys. 55 (1964) 673; F. G. Perey and B. Buck, Nucl. Phys. 32 (1962) 353; F. G. Perey, Phys. Rev. 131 (1963) 745; G. R Satchler, Nucl. Phys. 70 (1965) 177.
13. W. J. Swiatecki, private communication (1978).
14. S. E. Vigdor et al., "Energy Dependence of the Fusion and Elastic Scattering of $^{16}O + ^{40}Ca$," preprint (1978) unpublished.
15. H. C. Britt et al., Phys. Rev. C13 (1976) 1483.
16. H. C. Britt et al., Phys. Rev. Lett. 39 (1977) 1458.
17. F. Plasil et al., Phys. Rev. C18 (1978) 2603.
18. M. Blann et al. Phys. Rev. C19 (1979) 1288; F. Plasil et al. Phys. Rev. Lett. 40 (1978) 1164.

Figure Captions

Fig. 1. Regions of stability in the RLD x-y space. This figure and Figs. 2-4 are reporduced from LBL 1502 with kind permission of the authors. The abscissa (x) is the liquid drop fissility parameter characteristic of the A and Z of the nuclide of interest. The ordinate is related to the square of the angular momentum. The limits of stability are $y < y_I$, oblate, $y_I < y < y_{II}$ prolate or triaxial, and $y > y_{II}$ unstable to fission. The y_{III} line represents stability ($y > y_{III}$) against asymmetry.

Fig. 2. Equilibrium ground and saddle point shapes for several values of the angular momentum for a nucleus near ^{56}Ni. The axis of rotation is indicated, as well as the shape for the ground states. The higher deformation in each case represents the saddle point shape.

Fig. 3. As in Fig. 2 for a nucleus near ^{149}Tb.

Fig. 4. Relationship of principal axis ratios to spherical radii versus x and y in the RLD. The interpretation of the curves is given in Sect. II.

Fig. 5. Qualitative properties of level densities in the E vs J space. The lower portion shows the position of the yrast and saddle point energies for a ^{58}Ni nucleus according to the RLD. Lines A and B are indicated, and the form of the level density along these cuts is shown in the upper portion of the figure.

Fig. 6. The E vs J space for ^{56}Ni. The yrast line is from RLD. The circle represents the compound nucleus excitation (ordinate) for 214 MeV ^{16}O on ^{40}Ca, for a 55 $\hbar$ partial wave in the entrance channel. The solid line represents the loci of minimum residual angular momenta and excitation when 9 to 39 MeV α particles are emitted, with

Figure Captions

T_ℓ from the spherical SCO model. The dashed curve represents the same for the deformed SCO model. The effective excitation energies above the yrast line are indicated for several kinetic energies. Triangles below the yrast lines contrast the differences in minimum and maximum residual excitations for the two sets (spherical and deformed) of calculations

Fig. 7. As in Fig. 6, for the ^{149}Tb nucleus formed by 236 MeV ^{40}Ar + ^{109}Ag.

Fig. 8. Illustration of logic of the Hauser-Feshbach code ALERT which was used in calculations presented herein. The control sequence and mesh sizes are discussed in Sect. III.

Fig. 9. Comparisons of several sets of transmission coefficients calculated for 30 MeV α particles incident on ^{52}Fe. Solid lines are for spherical systems, dashed lines for deformed systems. Results are shown for the SCO model and the optical model, plotted as T_ℓ vs partial wave (abscissa). The deformed nucleus is at 55 $\hbar$.

Fig. 10. Comparison of T_ℓ (ordinate) for 3 MeV neutrons and 15 MeV protons from ^{56}Ni vs partial wave ℓ. Results are from the SCO model for spherical and deformed (55 $\hbar$) nuclei.

Fig. 11. Comparison of radius (R/Ro) and potential (V/Vo) ratios of a deformed nucleus to those of a spherical nucleus (ordinate) versus position along the symmetry axis (abscissa). The nucleus considered is ^{149}Tb at 85 $\hbar$.

Fig. 12. Ratio to spherical of radii and potential for ^{149}Tb nuclei vs angular momenta (abscissa). Values of R and V were calculated as shown by the small open and closed points. The shapes of some of the nuclei are shown superimposed on a spherical projection of the same volume

Figure Captions

nucleus. The oblate and prolate/triaxial regions are indicated, as well as the values of the angular momentum for which the RLD predicts fission barriers of zero and 8 MeV.

Fig. 13. As in Fig. 12 for the ^{56}Ni nucleus.

Fig. 14. Calculated branching ratios for the deexcitation of ^{149}Tb at 120 MeV of excitation vs initial angular momentum. The open circles near the abscissa represent the values of compound nucleus angular momenta for which results were calculated. Smooth curves were drawn through these points. Fission curves (f) represent total fission, whereas n,p,α curves represent only first chance emission. Curves are for spherical (solid lines) and deformed nuclei (dashed lines).

Fig. 15. As in Fig. 14 for decay of ^{56}Ni.

Fig. 16. Maximum angular momenta deduced from γ-ray multiplicity and evaporation residue excitation function measurements. These curves are reproduced from Ref. (15) with permission of the authors. This figure is discussed in Sect. V.

Fig. 17. First chance α spectra calculated for decay of ^{149}Tb for different entrance channel angular momenta. The most probable kinetic energies are shown by each spectrum. All spectra are computed using T_ℓ for deformed nuclei using the SCO model, except for the lower curve for $I = 95\ \hbar$, for which spherical nucleus T_ℓ (SCO) were used.

Fig. 18. First chance α spectra calculated for decay of ^{56}Ni at 172 MeV excitation using spherical and deformed SCO transmission coefficients. The compound nucleus angular momentum for which each spectrum was computed is shown by the spectrum.

Fig. 19. Representation of branching for multiple particle emission from ^{56}Ni at 55 $\hbar$ and 172 MeV of excitation. The partial reaction cross

Figure Captions

section of 42 mb divides as shown by the histograms. Approximate emission cross sections from various nuclides are shown above the histograms. The shaded bar graphs at the lower portion of the figure indicate that 31 of 42 mb are calculated as going into fission for this example, using T_ℓ calculated with SCO for spherical nuclei.

Fig. 20. As in Fig. 19, but calculated using T_ℓ calculated with the spherical optical model.

Fig. 21. As in Fig. 19, but calculated using SCO deformed nucleus T_ℓ values. Note the virtual disappearance of fission, and dominance of α emission.

Fig. 22. As in Fig. 19, but calculated using the T_ℓ resulting from the deformed optical model

Fig. 23. As in Fig. 21 but for a ^{56}Ni compound nucleus at 45 MeV.

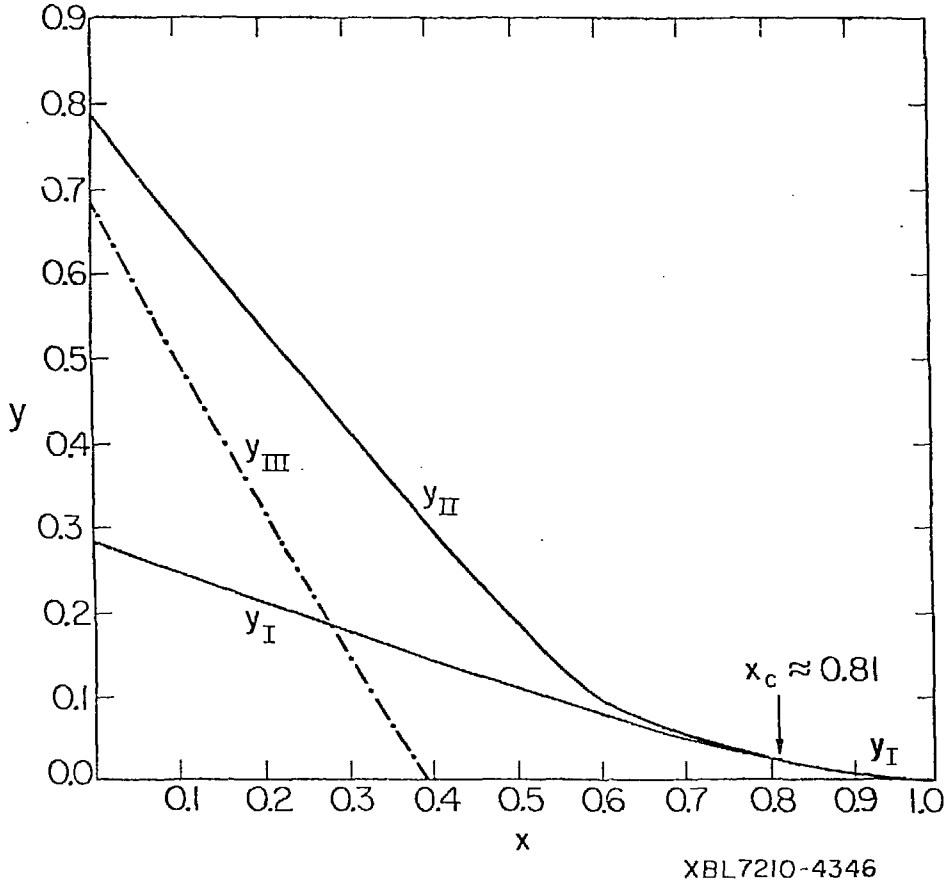
0.9
0.8
0.7
0.6
0.5
0.4
0.3
0.2
0.1
0.0
y
0.1
0.2
0.3
0.4
0.5
0.6
0.7
0.8
0.9
1.0
x
y_{III}
y_{II}
y_I
$x_c \approx 0.81$
y_I
XBL7210-4346

Figure 1

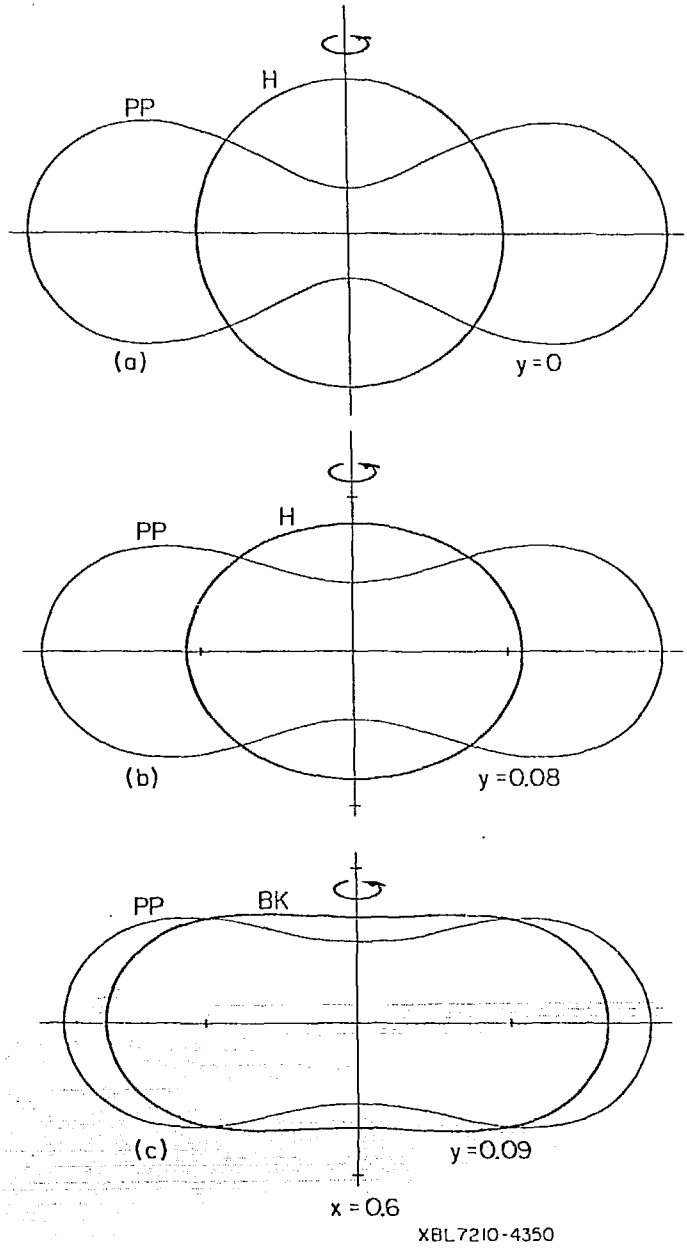

Figure 3

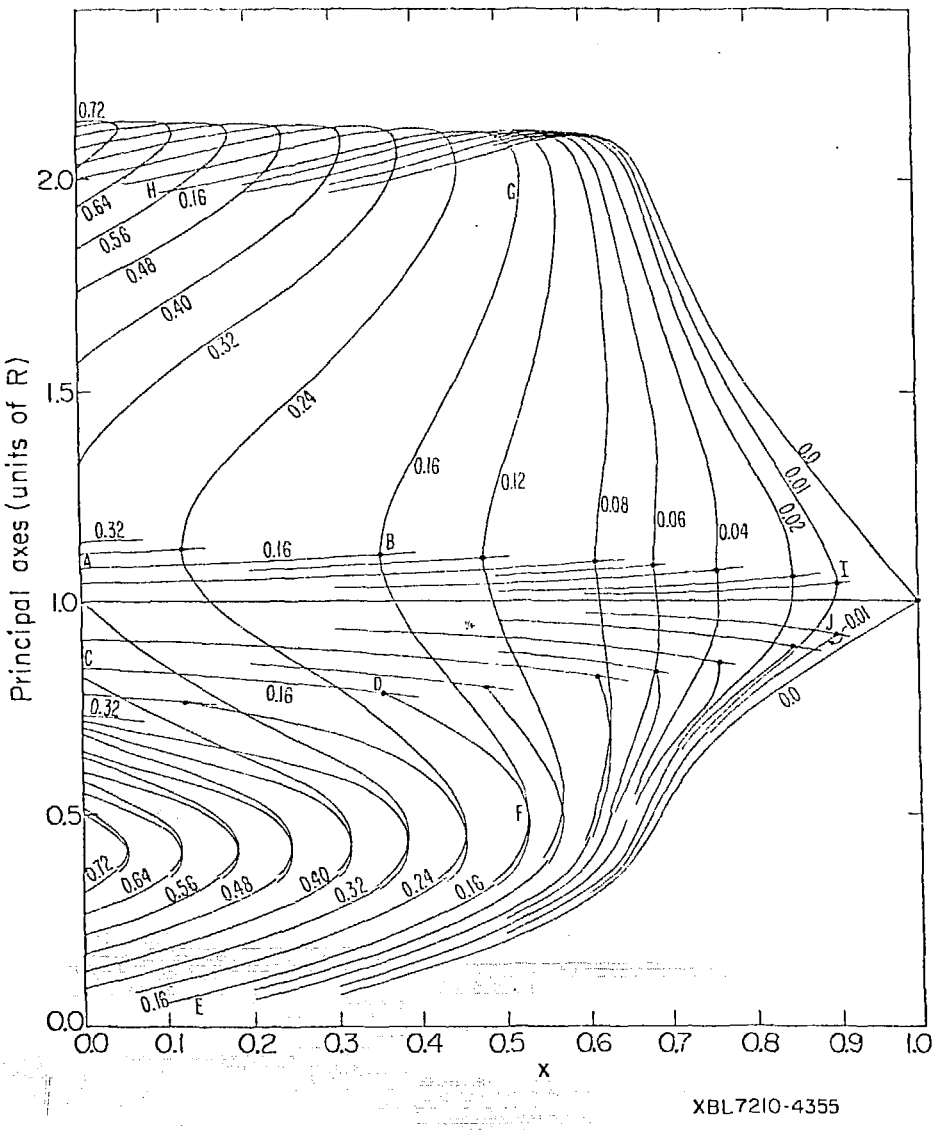
Principal axes (units of R)
x
0.0
0.5
1.0
1.5
2.0
0.1
0.2
0.3
0.4
0.5
0.6
0.7
0.8
0.9
1.0
0.72
0.64
0.56
0.48
0.40
0.32
0.24
0.16
0.12
0.08
0.06
0.04
0.02
0.01
0.0
-0.01
A
B
C
D
E
F
G
H
I
J
XBL7210-4355

Figure 4

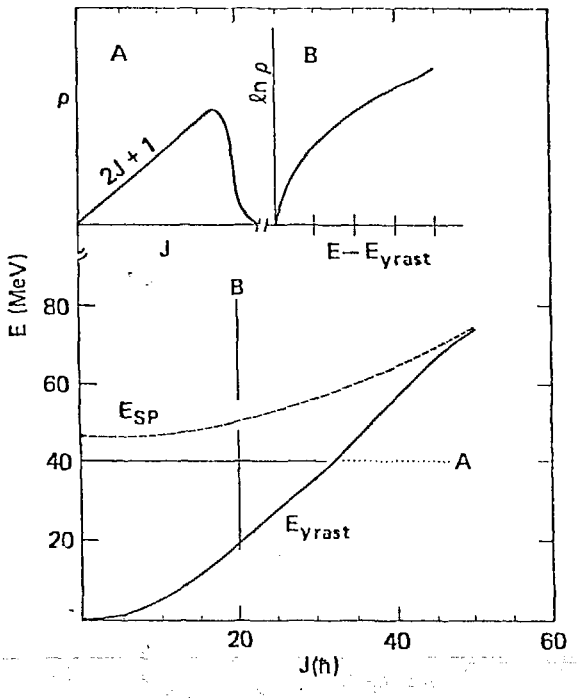

Figure 5

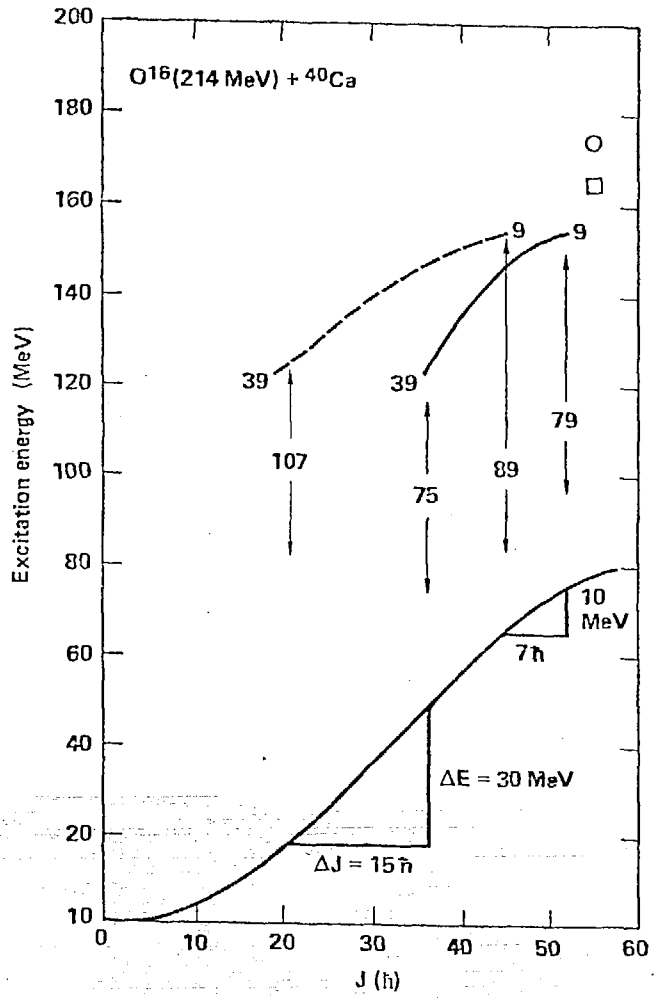
O16(214 MeV) + 40Ca
Excitation energy (MeV)
J (ħ)
39
107
39
75
9
89
9
79
10 MeV
7ħ
ΔE = 30 MeV
ΔJ = 15ħ

Figure 6

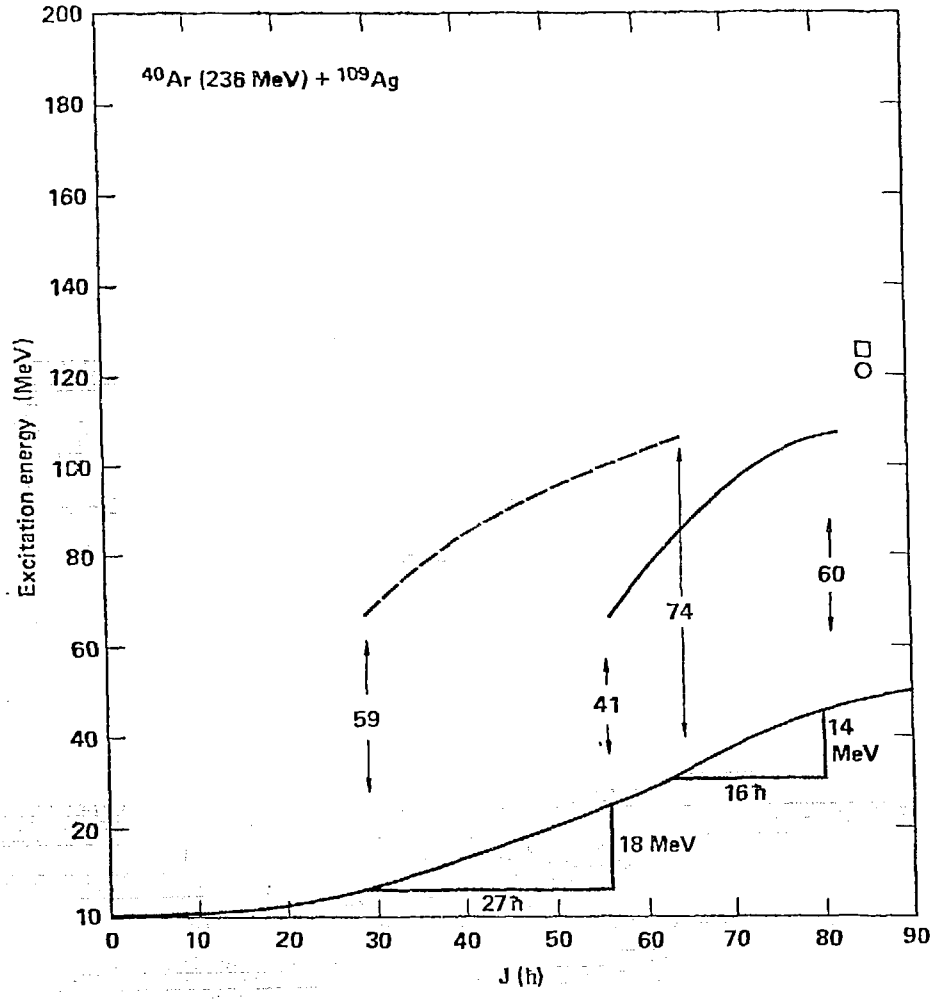
^{40}Ar (236 MeV) + ^{109}Ag
Excitation energy (MeV)
J (ħ)
59
41
74
60
14 MeV
16 ħ
18 MeV
27 ħ

Figure 7

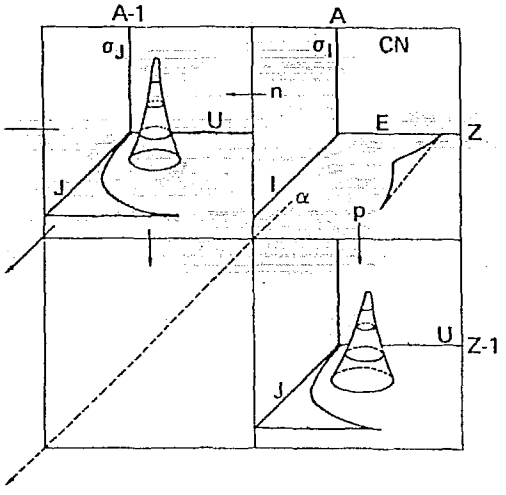

Figure 8

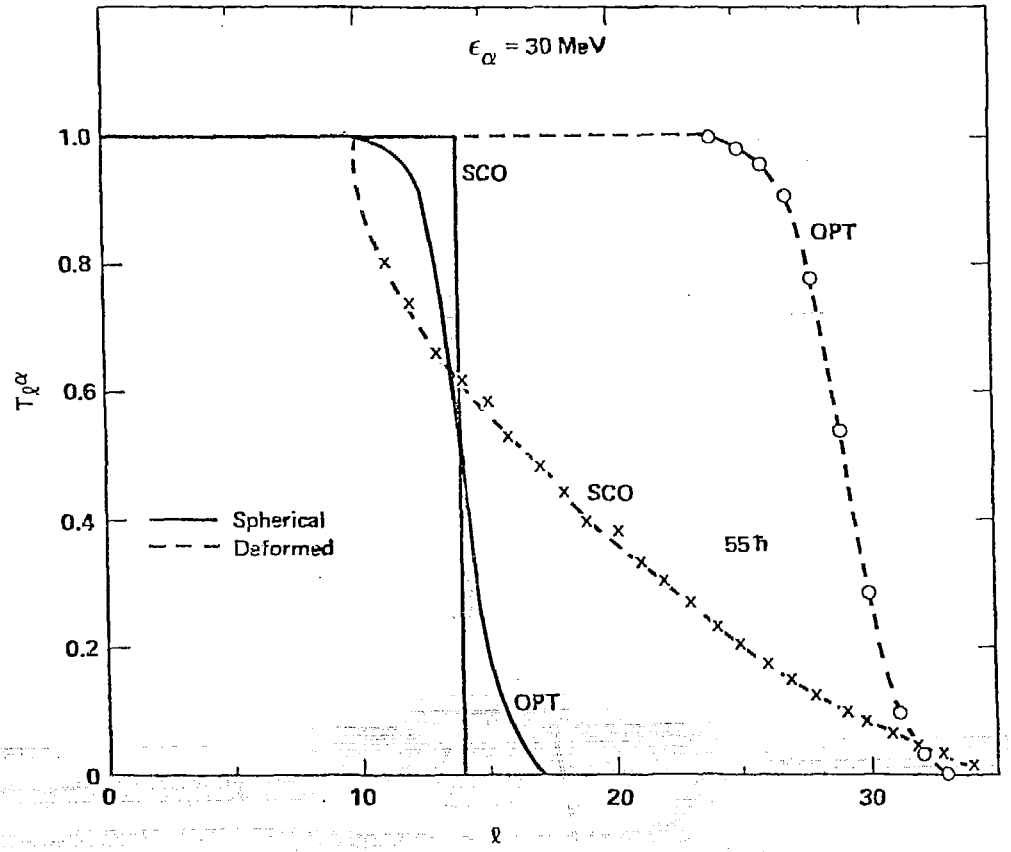
ϵ_α = 30 MeV
1.0
0.8
0.6
0.4
0.2
0
T_ℓ^α
SCO
OPT
SCO
55ħ
OPT
Spherical
Deformed
0
10
20
30
ℓ

Figure 9

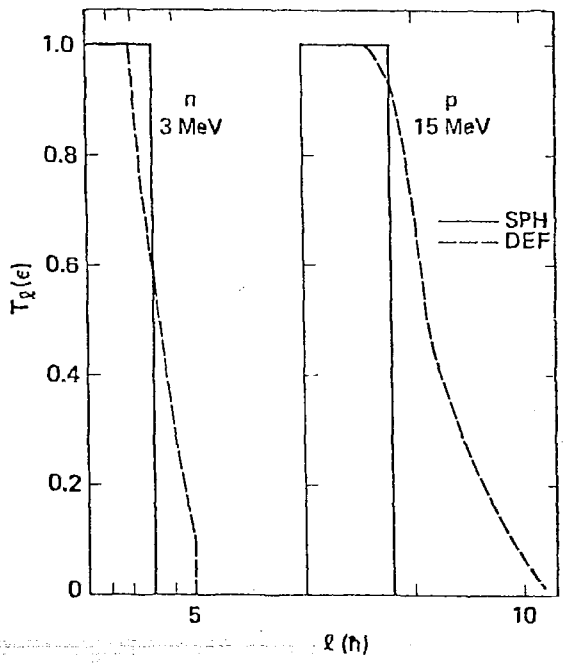

Figure 10

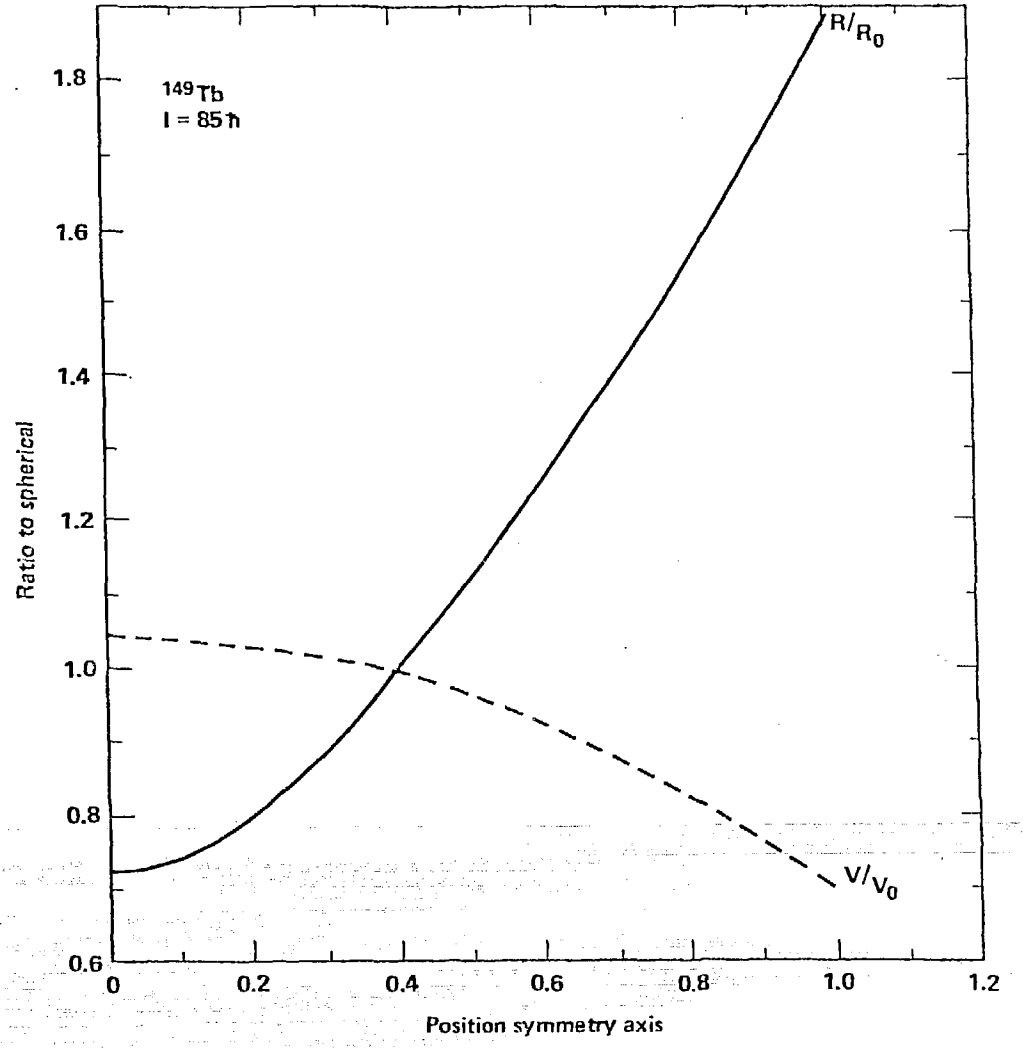
^{149}Tb
I = 85 ħ
R/R$_0$
V/V$_0$
Ratio to spherical
Position symmetry axis
1.8
1.6
1.4
1.2
1.0
0.8
0.6
0
0.2
0.4
0.6
0.8
1.0
1.2

Figure 11

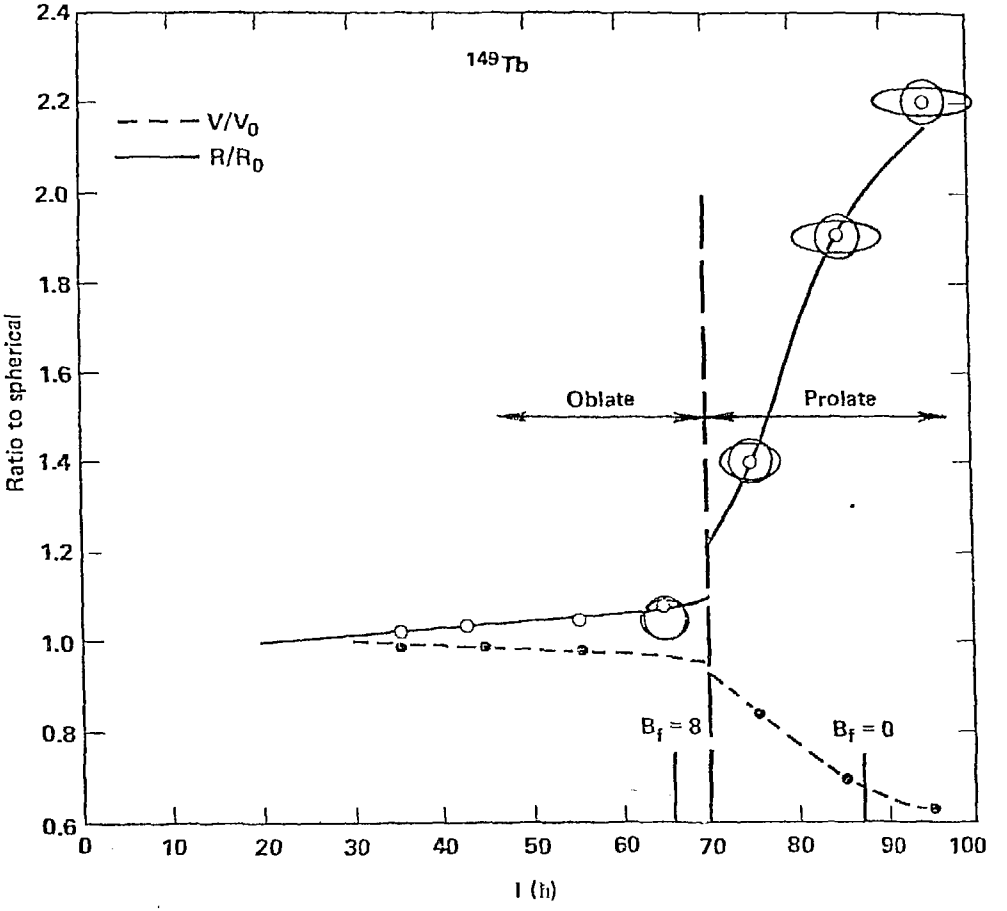
149Tb
V/V0
R/R0
Oblate
Prolate
Bf = 8
Bf = 0
Ratio to spherical
I (ħ)
2.4
2.2
2.0
1.8
1.6
1.4
1.2
1.0
0.8
0.6
0
10
20
30
40
50
60
70
80
90
100

Figure 12

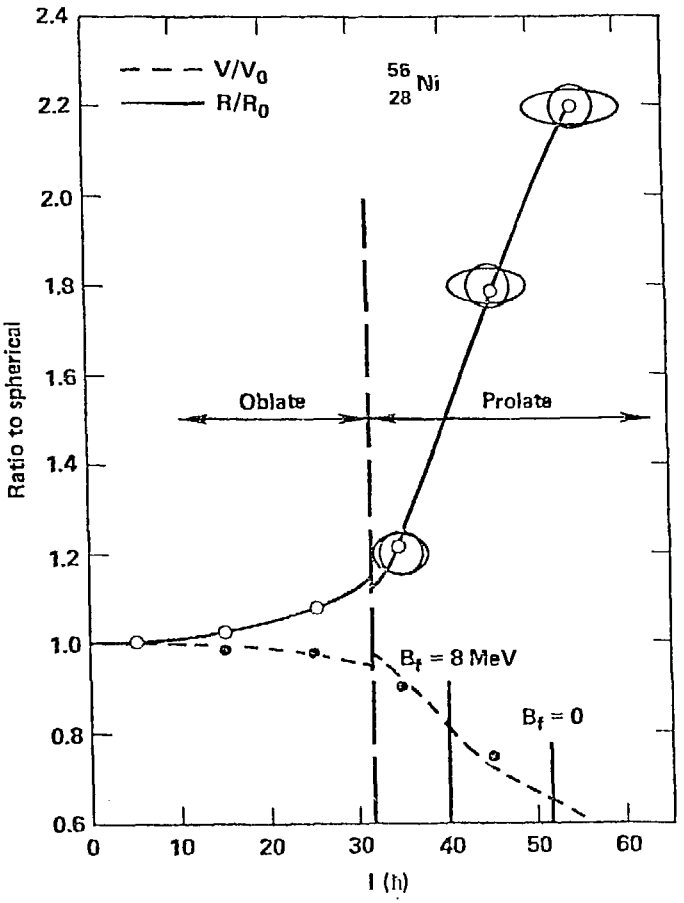
2.4
2.2
2.0
1.8
1.6
1.4
1.2
1.0
0.8
0.6
Ratio to spherical
V/V0
R/R0
56 28 Ni
Oblate
Prolate
Bf = 8 MeV
Bf = 0
0
10
20
30
40
50
60
I (ħ)

Figure 13

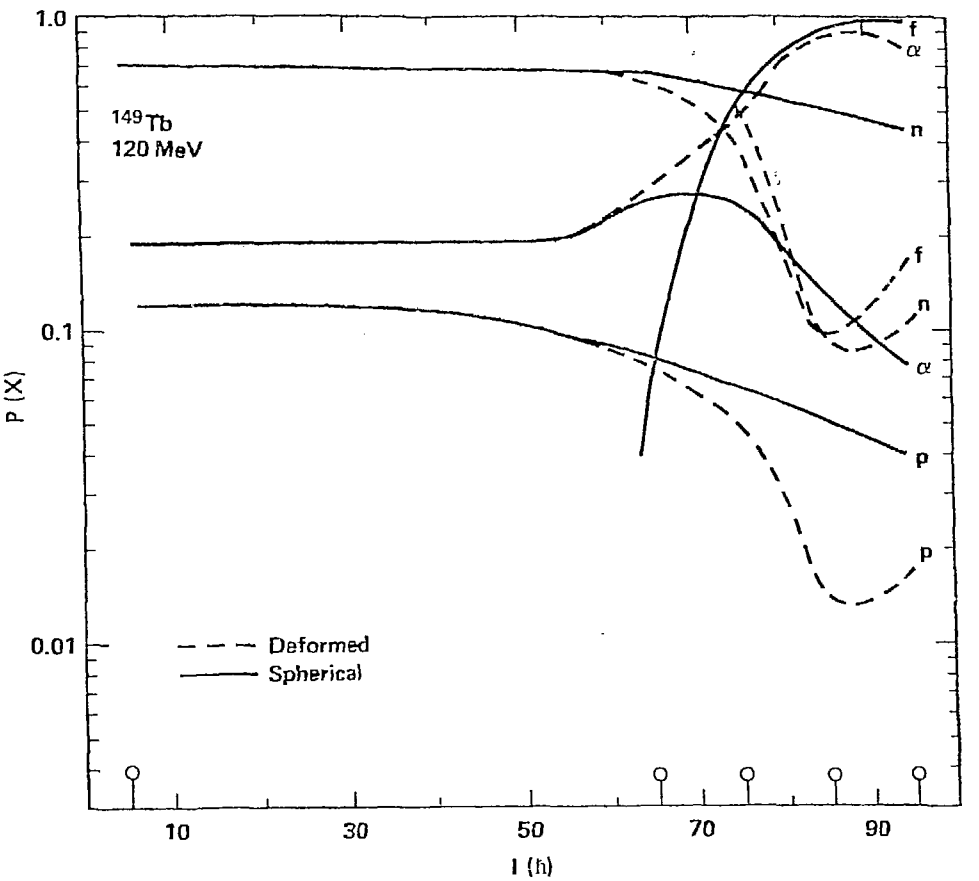
1.0
0.1
0.01
P (X)
149Tb
120 MeV
f
α
n
f
n
α
p
p
Deformed
Spherical
10
30
50
70
90
I (ħ)

Figure 14

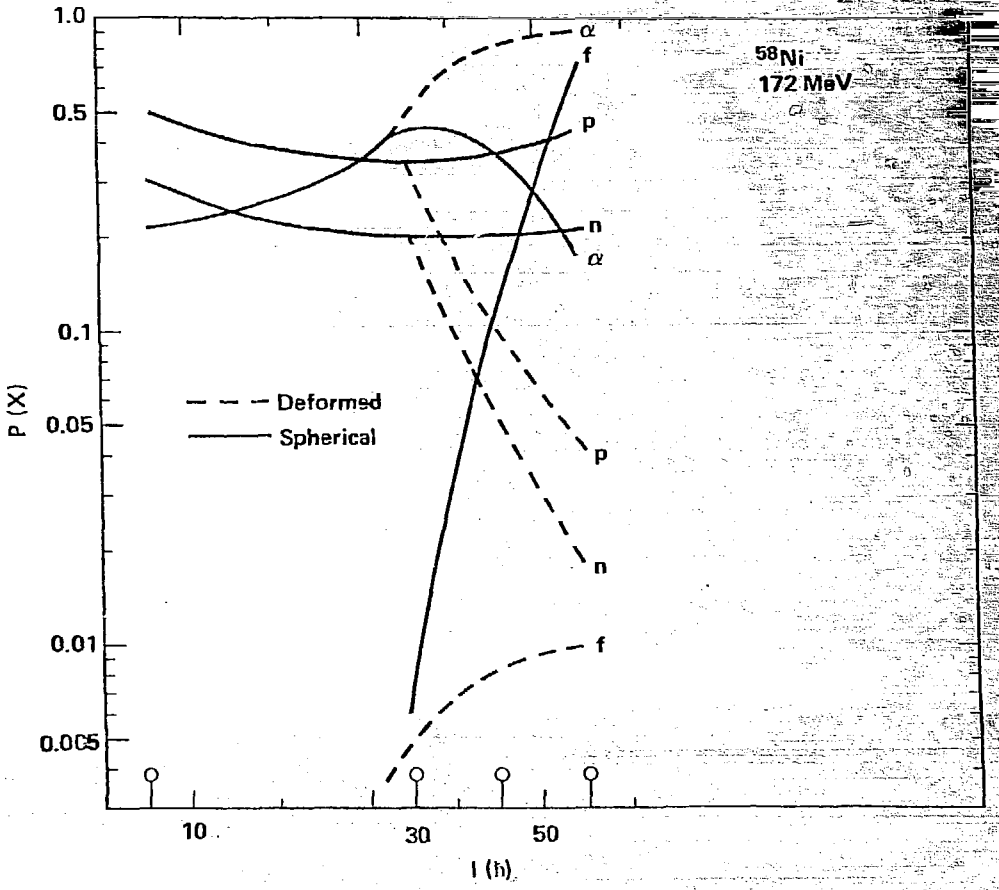
1.0
0.5
0.1
0.05
0.01
0.005
P (X)
10
30
50
l (ħ)
α
f
p
n
α
p
n
f
Deformed
Spherical
58Ni
172 MeV

Figure 15

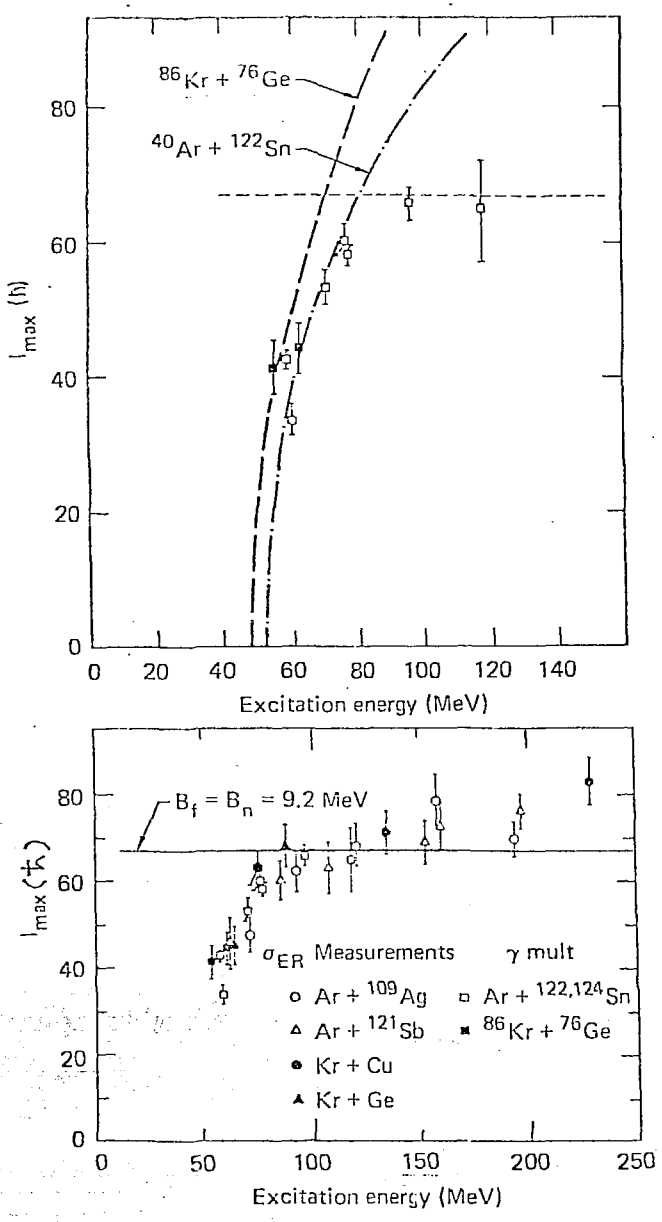
$^{86}Kr + ^{76}Ge$
$^{40}Ar + ^{122}Sn$
I_{max} (ħ)
Excitation energy (MeV)
$B_f = B_n = 9.2$ MeV
σ_{ER} Measurements
γ mult
Ar + ^{109}Ag
Ar + ^{122,124}Sn
Ar + ^{121}Sb
$^{86}Kr + ^{76}Ge$
Kr + Cu
Kr + Ge

Figure 16

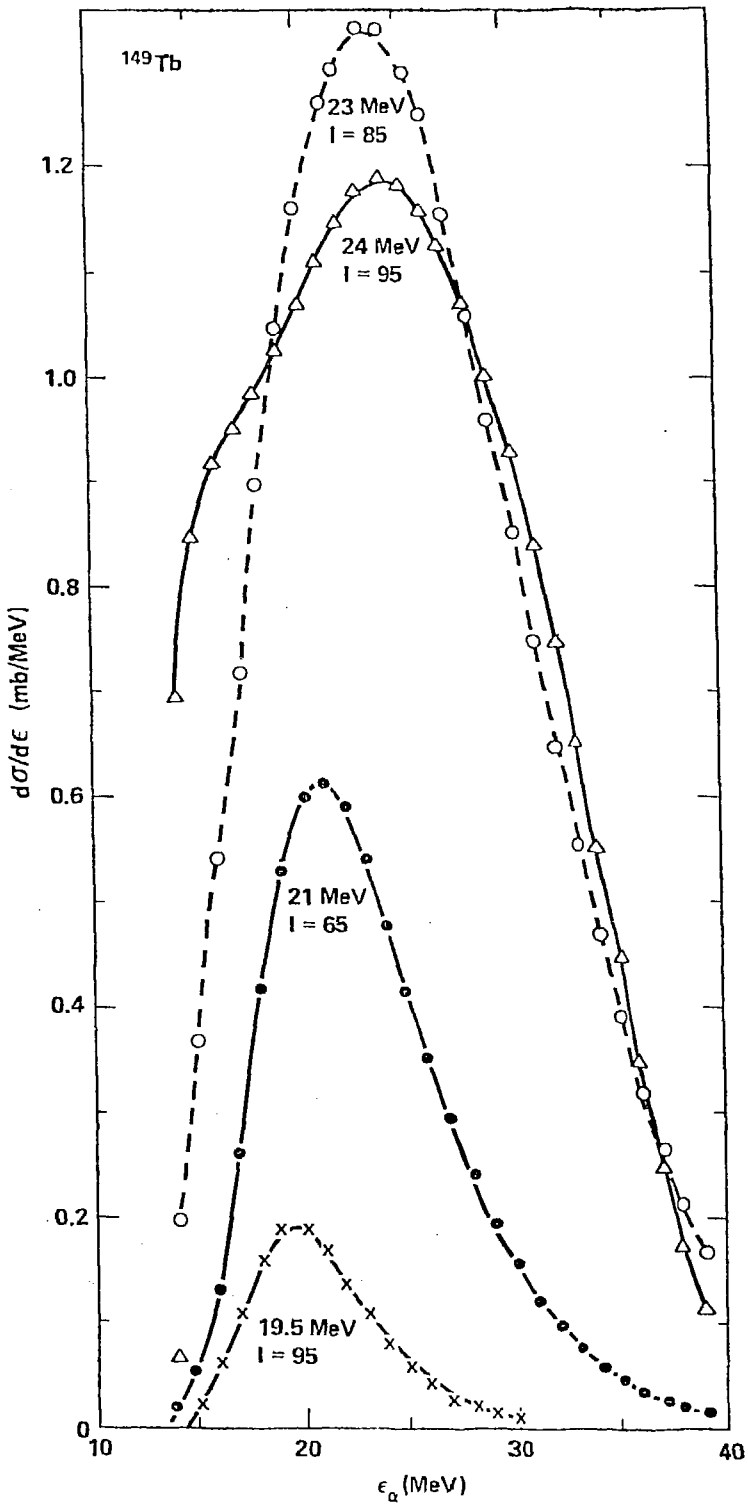
149Tb
23 MeV
l = 85
24 MeV
l = 95
21 MeV
l = 65
19.5 MeV
l = 95
dσ/dε (mb/MeV)
εα (MeV)
0
0.2
0.4
0.6
0.8
1.0
1.2
10
20
30
40

Figure 17

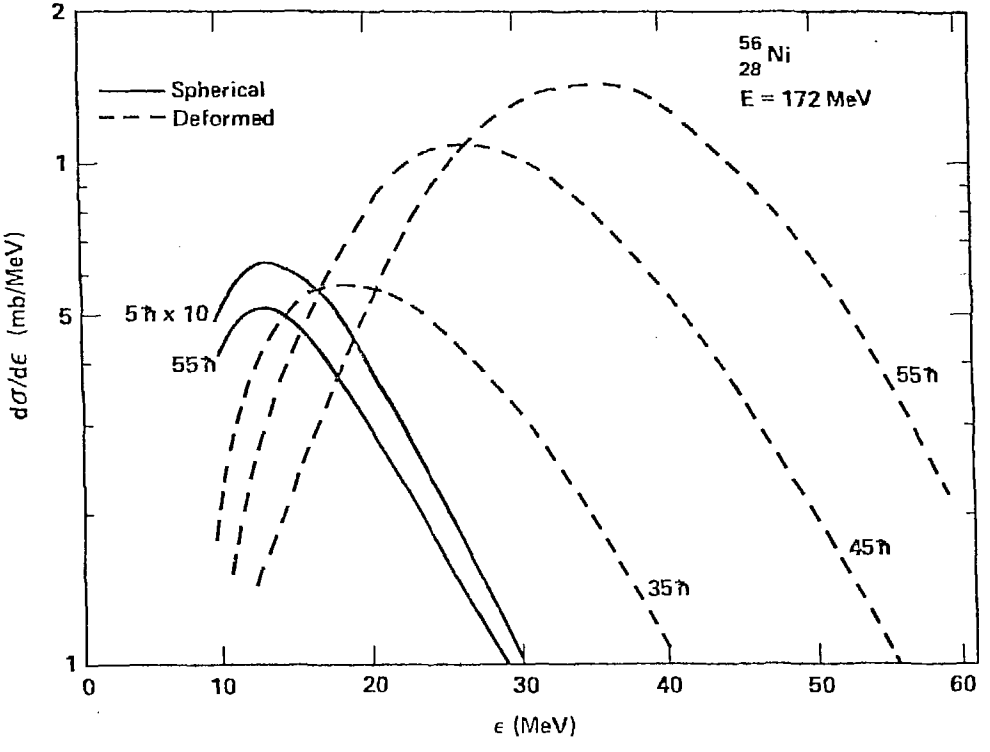
2
1
5
1
0
10
20
30
40
50
60
dσ/dε (mb/MeV)
ε (MeV)
Spherical
Deformed
56 28 Ni
E = 172 MeV
5ħ x 10
55ħ
55ħ
45ħ
35ħ

Figure 18

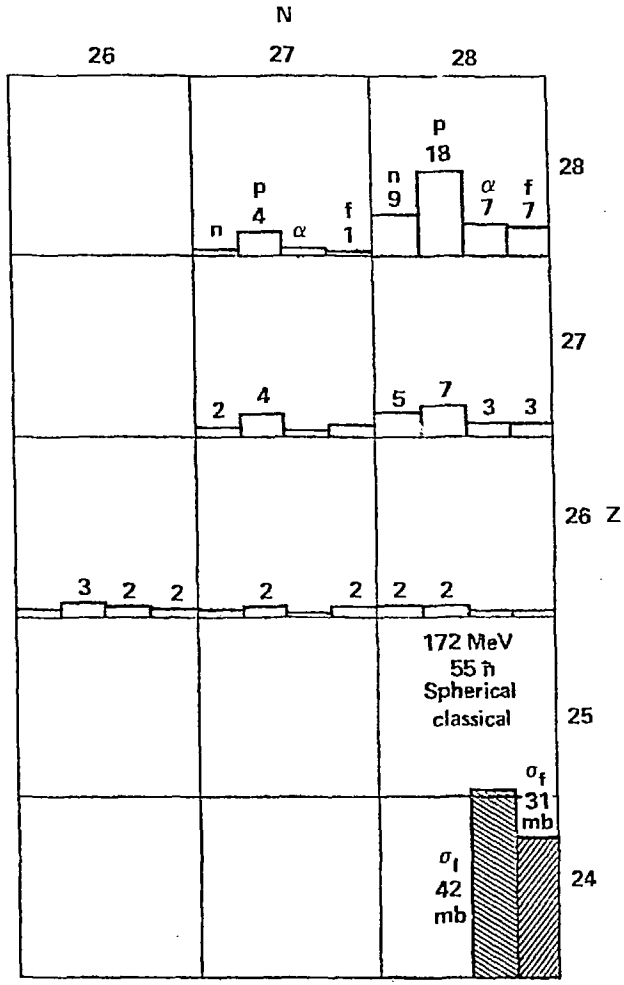
N
26
27
28
p
18
n
9
α
7
f
7
p
4
n
α
f
1
28
27
2
4
5
7
3
3
26 Z
3
2
2
2
2
2
2
172 MeV
55 ħ
Spherical
classical
25
σ_f
31
mb
σ_l
42
mb
24

Figure 19

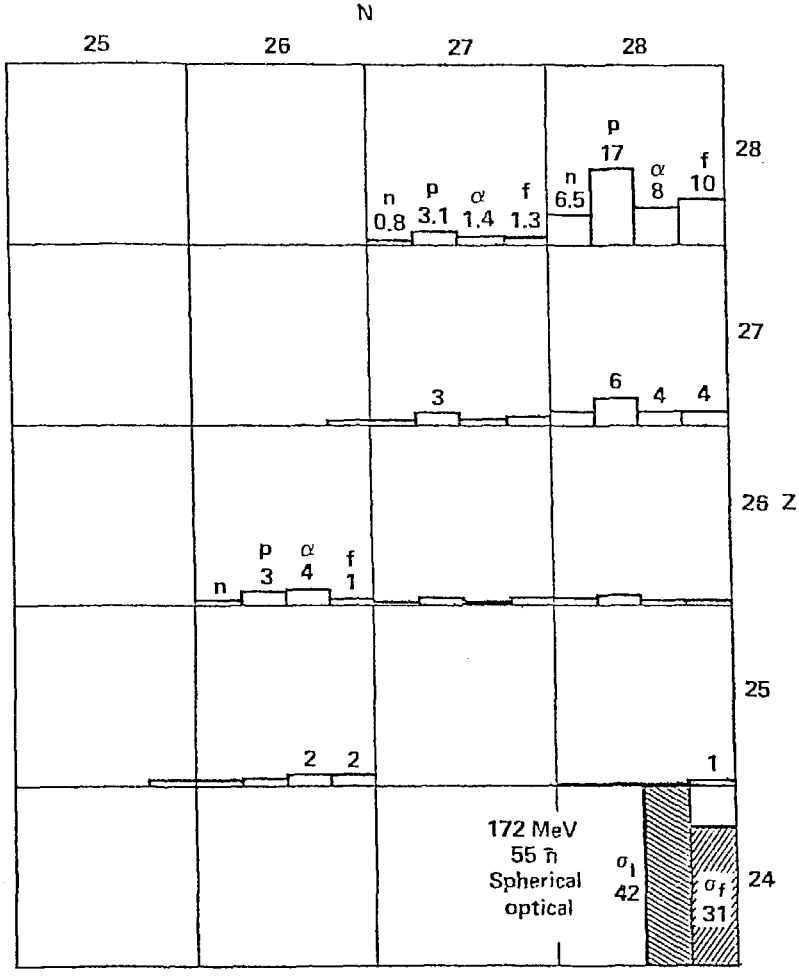
N
25
26
27
28
n 0.8
p 3.1
α 1.4
f 1.3
n 6.5
p 17
α 8
f 10
28
3
6
4
4
27
n
p 3
α 4
f 1
26 Z
2
2
1
25
172 MeV
55 n̄
Spherical
optical
σ_I 42
σ_f 31
24

Figure 20

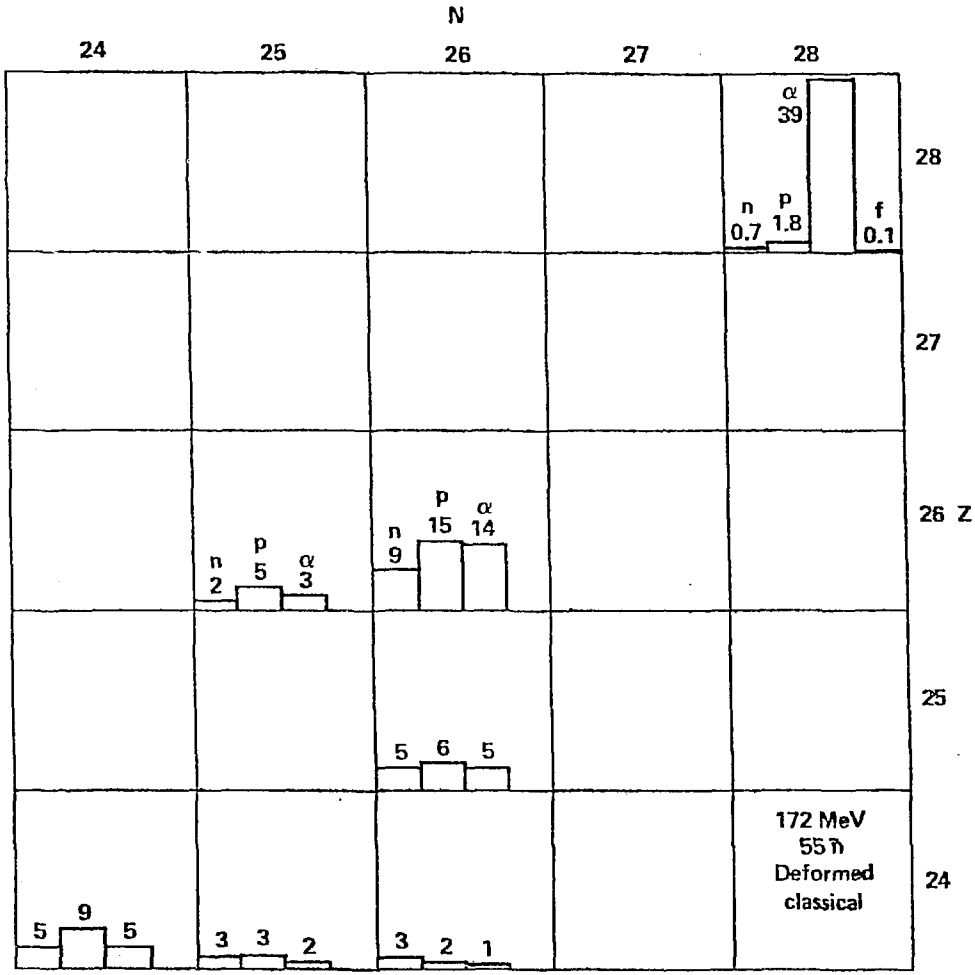
N
24
25
26
27
28
α
39
n
0.7
p
1.8
f
0.1
28
27
n
2
p
5
α
3
n
9
p
15
α
14
26 Z
5
6
5
25
172 MeV
55 ħ
Deformed
classical
24
5
9
5
3
3
2
3
2
1

Figure 21

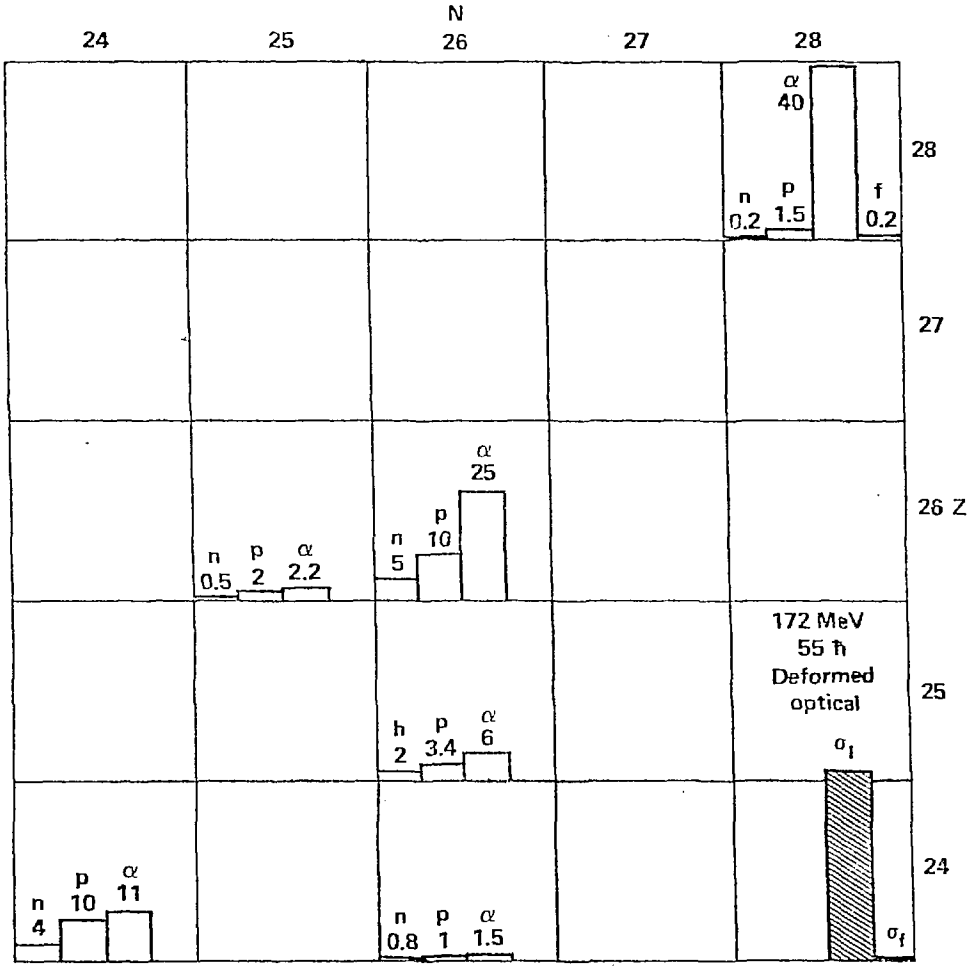
N
24
25
26
27
28
α
40
n
0.2
p
1.5
f
0.2
28
27
α
25
p
10
n
5
n
0.5
p
2
α
2.2
26 Z
172 MeV
55 ħ
Deformed
optical
25
h
2
p
3.4
α
6
σ_I
p
10
α
11
n
4
n
0.8
p
1
α
1.5
σ_f
24

Figure 22

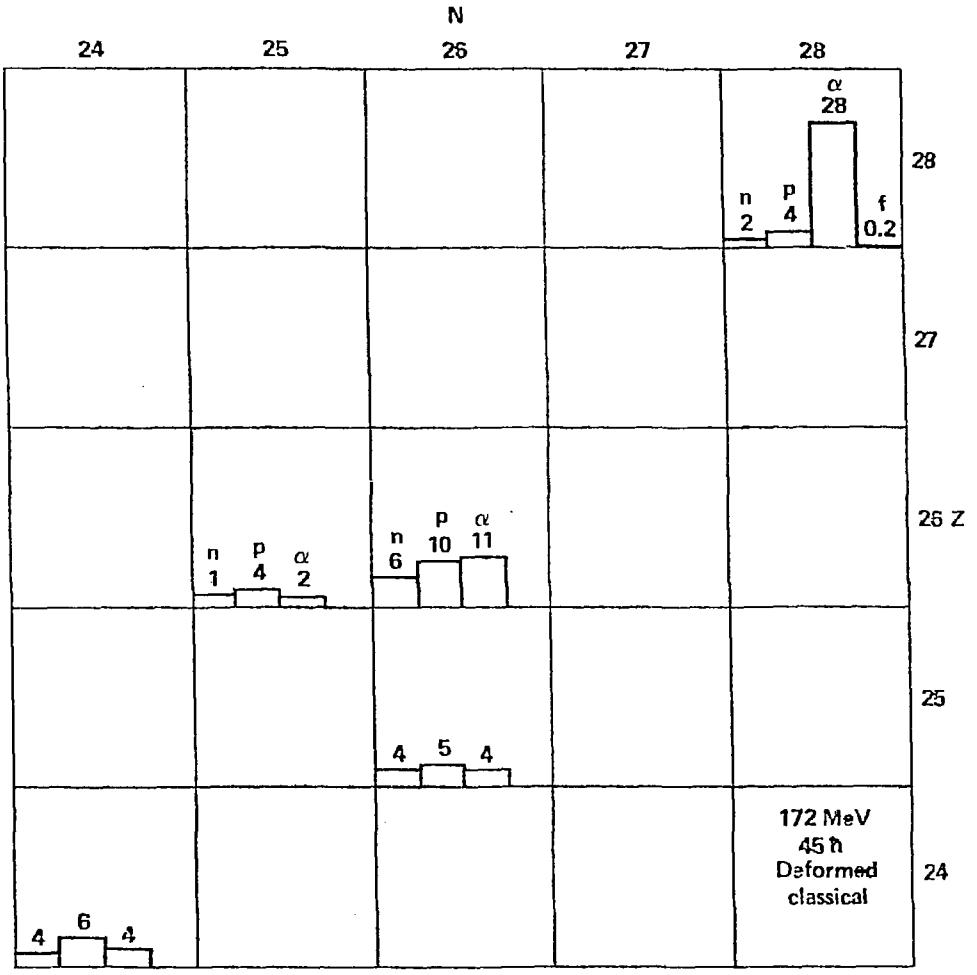
N
24
25
26
27
28
α
28
n
2
p
4
f
0.2
28
27
n
1
p
4
α
2
n
6
p
10
α
11
26 Z
25
4
5
4
25
172 MeV
45 ħ
Deformed
classical
24
4
6
4
24

Figure 23